We responded to all the comments by the reviewer. The criticism and suggestions by the reviewer were appropriate and improved the quality of our manuscript. We appreciate such efforts.

Authors′ response to reviewers′ comments

Paper No.: acp-2016-1181
Title: **Depolarization Ratios Retrieved by AERONET Sun/Sky Radiometer Data and Comparison to Depolarization Ratios Measured With Lidar**

Revision of the paper

Reviewer #2

General comments

This article addresses a problem of dust particles detection in the atmosphere, which is of high interest of scientific community. A new method for quantitative estimation of dust presence based on particle depolarization ratio retrieved from AERONET inversion is suggested. Authors made significant efforts to evaluate the AERONET retrieved particles depolarization ratio by comparing them with ones measured with lidar. To do so a vertical profile of particle depolarization ratio retrieved from lidar measurements is column-integrated using a weighting function. To my knowledge this work shows one of the few positive results of such comparison. I would recommend this paper for publication, given that authors will address the issues listed below.

Specific comments

1. The general idea of evaluating depolarization ratio retrieved from AERONET by comparison with lidar retrieved values implies that lidar retrievals are well evaluated. I think that such implication is not properly supported in the paper.

: As reviewer suggested, description of the depolarization ratio calibration has been included in the revised manuscript in the line from 218 - 234.

"In order to obtain reliable depolarization ratios, the data of the lidar measurements must be calibrated before physical quantities such as the linear volume depolarization ratio can be retrieved. It is important to calibrate the signal intensities of the $P_{\parallel}$ and $P_{\perp}$ first, before the linear volume depolarization ratio is calculated. Thet calibration method of the lidar system is explained in detail by Shimizu et al. (2017) and Nishizawa et al. (2017).

The difference of the sensitivity between two PMTs that are used by the lidar system to detect these components is checked regularly by the following method. A sheet polarizer whose polarizing direction is set at 45° to the polarizing plane of the emitted light is inserted in front of the beam

splitter cube, and the backscatter signal from the sky is recorded as a reference signal. In this reference record, the light intensities of the two channels are equal after the sheet polarizer, so the calibration constant can be obtained by comparing the recorded values of $P_{||}$ and $P_{\perp}$. In the next step, the sheet polarizer is rotated by 90° which sets the polarizing angle at −45°, and another reference signal is recorded. Then relative calibration of $P_{||}$ and $P_{\perp}$ channels using signals measured for the polarizing angles at ± 45°. This pair of reference signals reduces any error caused by a poor positioning of the sheet polarizer (Freudenthaler et al., 2009; 2016). The reference signals are usually recorded once per year for each lidar (Shimizu et al., 2017)."

2. The depolarization ratio defined from AERONET retrievals by eq. 1 has a meaning of $\frac{\beta_{P,\perp}}{\beta_{P,11}}$. Justification needed why this parameter is compared with one retrieved from lidar (eq. 4), which is not the same physical value.

: The depolarization ratio by lidar measurements can also calculated according to $\frac{\beta_{P,\perp}}{\beta_{P,11}}$. The previous expression of $\delta^{L}(z) = \frac{P_{\perp}(z)}{P_{||}(z) + P_{\perp}(z)}$ is changed to $\delta^{L}(z) = \frac{P_{\perp}(z)}{P_{||}(z)}$.

3. Page 11. Line 217. Molecular depolarization ratio is system dependent it is not clear if the value 0.0044 provided by Behrendt and Nakamura suits the lidar system used.

: The molecular depolarization ratio of 0.0044 can be used to the optical filters with very small bandwidth and measure almost only central Cabannes line of Rayleigh scattering. It is for that reason that the value of 0.0044 is not the correct value. We checked the related thing and the value of 0.014 was applied in the research. We applied 0.014 in the calculation of depolarization ratio, but it is our mistake to have 0.0044 in the manuscript. It has been corrected.

4. **Page 11. Formula 7.** From the description it is not clear how aerosol backscatter coefficient is "measured".

Was Raman or Klett technique used?

If Klett, which lidar ratio was assumed?

If Raman, which angstrom was used?

Do these values suit dust particles? Also it is not clear how their selection influences the column-integrated depolarization ratio estimated from lidar, if any of the methods was applied.

: The backscatter coefficient was calculated by Fernald's method. And the lidar ratio of 50 sr is applied in the calculation. The value of the lidar ratio is important to calculate the exact value of the aerosol backscatter and extinction coefficients. However, the aerosol backscatter coefficient was used to obtain the ratio of the vertical distribution of aerosols in this research. The related explanation was added in the manuscript in line 261-272.

"The aerosol backscatter coefficient is derived by the backward version of Fernald's method (Fernald, 1984). The data observed at 9 km height are used as reference height for the analysis of data taken under cloud-free conditions.

The reference height is lowered if the signal-to-noise ratio at 9 km is not sufficient which may be the case of high aerosol concentration. Molecular density profiles are taken from the COSPAR international reference atmosphere (CIRA-86) for computing the Rayleigh scattering component. A constant lidar ratio of 50 sr is applied in the calculation of the aerosol backscatter coefficients (Shimizu et al., 2017). Since the lidar ratio differs for different aerosol types, the selection of the lidar ratio is important to obtain exact values of extinction and backscatter coefficients. However, we only use the ratio of the backscatter coefficient in the calculation of W(z) in our study. For that reason, the value of the lidar ratio does not affect the calculation of W(z)."

Technical issues

Page 2. Line 42-43. "Decreases with increasing" and "In contrast … increases with decreasing" describe the same situation. Should be "increases with increasing", I presume.

: As reviewer suggested, the sentence " increases with decreasing" has been changed as " increases with increasing" in the revised manuscript.

Page 3. Line 67. "global atmosphere", I think simple "atmosphere" would be enough.

: "global" has been removed in the revised manuscript.

Page 4. Line 76. "desert dust and other anthropogenic …". Usage of "other" implies that dust I s also anthropogenic, consider removing it.

: "other" has been removed in the revised manuscript.

Page 4. Line 78 & 80. "typical radius" instead of "typically".

: It has been changed as reviewer suggested.

Page 4. Line 83. "we'll" instead of "we" for conditional clause.

: It has been changed as reviewer suggested.

Page 4. Line 90. Space is missing in “lidar.The”

: It has been corrected.

Page 14. Lines 296–299. “Values of …from both instruments”. It is not clear that authors are discussing results of Muller et al 2012.

: It has been changed as below in the revised manuscript in line 416 - 421.

“Müller et al. (2010; 2012) compared those data with data derived from collocated AERONET Sun/sky radiometer observations. Values of δ_p from both instruments agree at 1064-nm wavelength (Müller et al., 2010; 2012). If the Sun/sky radiometer results are extrapolated to the lidar wavelength of 355 nm, the value of δ_p obtained from the Sun/sky radiometer is 20 % lower than the value obtained from the lidar observations, see Figure 3 in Müller et al. (2010) and Figure 7 in Müller et al. (2012).”

Page 17. Description of figure 7. Figure 7 shows AERONET results and it is not indicated neither in the figure description in the text neither in the figure caption.

: The text “derived from the AERONET sun/sky radiometer measurements” has been added in the revised figure 7 caption.

Page 18. Line 368-369. Whole sentence “Dust particles are…” has no logical connection with the main paragraph describing optical properties of desert dust, consider removing.

: It has been removed in the revised manuscript.

Page 18. Line 382-383. “Except for SSA at 440 nm …” and “at each wavelength” in the same sentence are in logical contradiction. Consider reformulating or deleting “each wavelength”.

: “ at each wavelength” has been removed in the revised manuscript.

Page 20. Line 427. Description of the table containing abbreviations, and some of them (CMF) are not referenced earlier in the text. Please, indicate the meanings of symbols.

: It has been corrected.

Page 21. Line 447. “and/or a higher” change to “and/or by a higher”

: It has been corrected.

Page 22. Line 474. "…by the mixing of pollution …", maybe "… by the presence of pollution …" instead.

: It has been corrected.

Page 27. Line 576. "The average .. decreases as .. increases ". This phrase is too general. It is true for the values of Rvs and particle type discussed in the text, but generally the dependence is not monotonous. Consider reformulating.

:The relationship between volume median radius and δ_P^S retrieval has been newly discussed in section 3.1. in the revised manuscript. We can know through the discussion that volume median radius of fine-mode is strongly influencing δ_P^S at 440 nm. But, the volume median radius of coarse-mode is less affected than the fine-mode median radius. For that reason, we removed the sentence "The average Rv_c decreases as δ_P^S increases." in the revised manuscript.

Figure 3. AERONET does provide AOD at 500nm, but it is not "measured", it is "estimated" (or "retrieved") from measurements at 440, 670, 870 and 1020nm.

: Figure 3 caption has been changed.

Figure 6. Is it possible to make plots bigger? And since the plots are referenced by the number of the group, maybe, it'll be more logical to name plots 1a, 1b, 1c… 6a, 6b, 6c rather than a1, a2, a3, …. f1, f2, f3.

: It has been changed as reviewer suggested.

Figure 7. Please, mention in caption that SSA and SD are from AERONET.

: The figure caption has been corrected as "Average value of the SSA and the volume particle size distributions derived from the AERONET Sun/sky radiometer measurements for each of the 6 groups considered in this study: group 1 (black), group 2 (red), group 3 (blue), group 4 (pink), group 5 (gray), and group 6 (orange)."

Figure 9&11 Why only these figures have error bars? They are not discussed or mentioned in the text, are they necessary?

: The error bars have been removed in the revised manuscript.

Figure 12. Please, put legend "case 1" and "case 2" on the plots.

: It has been added.

We responded to all the comments by the reviewer. The criticism and suggestions by the reviewer were appropriate and improved the quality of our manuscript. We appreciate such efforts.

Authors′ response to reviewers′ comments

Paper No.: acp-2016-1181
Title: **Depolarization Ratios Retrieved by AERONET Sun/Sky Radiometer Data and Comparison to Depolarization Ratios Measured With Lidar**

Revision of the paper

Reviewer #2

Main comment:
This manuscript compares the particle linear depolarization ratio retrieved by AERONET with respect to the one measured by lidar. To this aim, a column-integrated depolarization ratio is retrieved from the lidar depolarization ratio since the AERONET depolarization ratio is column-integrated. From my point of view, the main achievements are the good correlation between both depolarization ratios using a considerable database from different stations and the parameter 'dust ratio' derived from the AERONET depolarization ratio. This 'new' parameter which can be used as proxy of the present of dust in the atmospheric column. The presented work is really interesting and it is a good contribution to the scientific community. Therefore, I recommend its publication. However, the authors should consider the following comments:

Major comments:
- Lidar depolarization measurements are used in this paper to validate the AERONET-derived depolarization ratio. Thus, the good lidar performance has to be demonstrated (it is used as reference!). However, only one line is dedicated to the technical specifications of the lidars (page 7 line 144) where two papers with more than 10 years are cited. The lidar depolarization technique had some advances in the last decade (from the 'polarization-dependent' of receiver transmission detected and corrected by Mattis et al., 2009 to the new theoretical framework and systematic-error estimation presented by Freudenthaler 2016; AMT and Bravo-Aranda et al., 2016; AMT). Thus, I suggest to include the depolarization calibration description in this paper highlighting the good performance.

: As reviewer suggested, description of the depolarization ratio calibration has been included in the revised manuscript in the line from 218 - 234.

"In order to obtain reliable depolarization ratios, the data of the lidar measurements must be calibrated before physical quantities such as the linear volume depolarization ratio can be retrieved. It is

important to calibrate the signal intensities of the $P_{\parallel}$ and $P_{\perp}$ first, before the linear volume depolarization ratio is calculated. Thet calibration method of the lidar system is explained in detail by Shimizu et al. (2017) and Nishizawa et al. (2017).

The difference of the sensitivity between two PMTs that are used by the lidar system to detect these components is checked regularly by the following method. A sheet polarizer whose polarizing direction is set at 45° to the polarizing plane of the emitted light is inserted in front of the beam splitter cube, and the backscatter signal from the sky is recorded as a reference signal. In this reference record, the light intensities of the two channels are equal after the sheet polarizer, so the calibration constant can be obtained by comparing the recorded values of $P_{\parallel}$ and $P_{\perp}$. In the next step, the sheet polarizer is rotated by 90° which sets the polarizing angle at −45°, and another reference signal is recorded. Then relative calibration of $P_{\parallel}$ and $P_{\perp}$ channels using signals measured for the polarizing angles at ± 45°. This pair of reference signals reduces any error caused by a poor positioning of the sheet polarizer (Freudenthaler et al., 2009; 2016). The reference signals are usually recorded once per year for each lidar (Shimizu et al., 2017).”

- It is stated that the lidar and AERONET depolarization ratio is well correlated. However, the correlation doesn’t occur at the ‘same’ wavelength. Why? I miss discussion in this way.

: The related discussion has been added in the revised manuscript in line 325 - 388.

“We tried to find the reason for the comparably low correlation at 440 nm. For that reason, we retrieved the δ_P^S at 532 nm by interpolating the value of δ_P^S at 532 nm on the basis of the four AERONET wavelengths. In the next step the differences between δ_P^S and δ_P^{CL} at 532 nm ($\delta_{P\ 532}^{CL} - \delta_{P\ 532}^{S}$) were calculated by deducting δ_P^{CL} (at 532 nm) from δ_P^S (at 532 nm) for all 580 cases for which we have δ_P^S at the four AERONET sites.

The values $\delta_{P\ 532}^{CL} - \delta_{P\ 532}^{S}$ of were varied from 0.14 to -0.09. In the following step the data were sorted according to the differences of $\delta_{P\ 532}^{CL} - \delta_{P\ 532}^{S}$. In the final step we divided these differences into intervals of 0.02, i.e. 1: >0.12, 2: 0.10 - 0.12, 3: 0.08 - 0.10, …, 11: -0.06 – (-0.08), 12: <(-0.08).

Figure 5 shows the variation of the averaged δ_P^S at the five wavelengths and the values of δ_P^{CL} at 532 nm divided by the differences of $\delta_{P\ 532}^{CL} - \delta_{P\ 532}^{S}$. The differences of δ_P^S between the wavelengths at 440 nm and 1020 nm are high.

We find that decreasing of δ_P^S with increasing wavelength if the value of $\delta_{P\ 532}^{CL} - \delta_{P\ 532}^{S}$ is low.

The differences between δ_P^S at 440 nm and δ_P^S at 1020 nm become less for increasing interval number, i.e. $\delta_{P\ 532}^{CL} - \delta_{P\ 532}^{S}$ for the interval number 7 (0 - 0.02); i.e. the yellow triangle pointing to the right . The value of δ_P^{CL} at 532 nm shows lower values than δ_P^S at 1020 nm in those intervals. The differences between δ_P^{CL} at 532 nm and δ_P^S at 1020 nm are reduced as the $\delta_{P\ 532}^{CL} - \delta_{P\ 532}^{S}$ is decreased up to the interval number 7 (0-0.02). We find an increasing of δ_P^S with increasing wavelength from the interval number 8 (0-(-0.02)) . The value of δ_P^{CL} at 532 nm is larger than the value of δ_P^S at 1020 nm in the interval number 8 (0-(-0.02)). Also, the differences between δ_P^{CL} at 532 nm and δ_P^S at 1020 nm as the interval number increased..

If we assume that the value of δ_P^{CL} at 532 nm is close to real value of δ_P, the results in Figure 5 indicate that the δ_P^S at 440 nm has been retrieved to be higher value than the δ_P^{CL} at 532 nm in the interval number from 1 (>0.12) to 7 (0-0.02) when the δ_P^{CL} at 532 nm showed low values (less than 0.08). Conversely, when the high δ_P^{CL} at 532 nm was measured, the δ_P^S at 440 nm showed a lower value than the δ_P^{CL} at 532 nm.

Figure 6 shows the average of volume particle size distributions of each interval data as separated in Figure 5. We see that the volume size distributions change from fine-mode dominated size distributions to coarse-mode dominated size distributions when the interval number moves from 1 (>0.12) to 12 (<(-0.08)).

The important point of Figure 6 is the variation of the volume median radius (Rv). The volume median radius of the coarse (Rv_c) and the fine (Rv_f) mode shows a maximum value at the interval number 1 (>0.12). Rv_f clearly and progressively decreases as the interval number moves from 1 (>0.12) to 12 (<(-0.08)). The Rv_f of the interval number 1 (>0.12) is two time larger than the interval number of 12 (<(-0.08)) as 0.28 ± 0.03 μm and 0.13 ± 0.01 μm, respectively. Rv_c also shows a pattern of decreasing values with decreasing values of $\delta_{P\ 532}^{CL} - \delta_{P\ 532}^{S}$. But it does not show as progressively as Rv_f.

Figures 5 and 6 show that the value of δ_P^S at 440 nm tends to be retrieved high for conditions where there is no dust at all or the dust concentration is low. Such conditions are usually dominated by a significant fine-mode of the particle size distribution.

When dust particles contribute the main share to the particle concentration, i.e. high values of δ_P^{CL} at 532 nm, the contribution of fine-mode particles is small. When particles in the fine-mode are the main contribution of the particle size distribution, i.e. low values of δ_P^{CL} at 532 nm, the size of the

particles in the fine-mode fraction are considered to have a large influence on the retrieval of the values of δ_P^S. This effect is considered to be more significant at 440 nm, i.e. at short wavelengths.

Mamouri and Ansmann (2017) found that the value of δ_P^L is maximum at 532 nm and lower at 355 and 1064 nm because of the competing influence the fine-mode and coarse-mode dust fraction have on the overall values (fine + coarse) of δ_P^L at the three wavelengths.

Haarig et al. (2017) found that on average the values of δ_P^L for aged Saharan dust were 0.25 at 355 nm, 0.31 at 532 nm, and 0.225 at 1064 nm. Müller et al. (2010; 2012) and Freudenthaler et al. (2009) also found spectral slope of the depolarization ratio with the maximum at 532 nm and lower values at 355 and 1064 nm during the Saharan Mineral Dust Experiment (SAMUM) 2006. The results clearly show a different pattern of the spectral variations of δ_P measured by lidar and retrieved from Sun/sky radiometer observations of dust.

It is a striking result that δ_P^S at 1020 nm, unlike δ_P^S at 440 nm, is very similar to the values of δ_P^{CL} at 532 nm. Though we cannot identify the reason for this similarity and even if the wavelengths (lidar at 532 nm and AERONET Sun/sky radiometer at 1020 nm) are different we may use the values of δ_P^S at 1020 nm as a qualitative indicator of the presence of mineral dust particles in the atmosphere. It remains open if we can use this parameter also as a qualitative measure of the mixing ratio of mineral dust and anthropogenic pollution particles compared to the more robust parameter δ_P^{CL} (at 532 nm)."

- Page 24 line 509: *'There is considerable evidence of the coating of dust particles by absorbing fine-mode pollution particles in the East Asian region'*. This sentence indicates that the 'internal mixing' is frequent(?) in the East Asian region but the presented method is based on external mixing. I miss some clarification in this regard. For example, May we say that the applicability of this method decreases with the 'flight time' of the transported dust layer? The sentence '*There is a higher possibility that pollutants can be mixed during long-range transport in case 2*' seems to point in this way. Is there any way to distinguish each situation (internal Vs external)?

: As reviewer commented, the discussion about "coating of dust particles by absorbing fine-mode pollution particle" can raise about internal mixing between dust and pollution particles. But, the method in this paper is based on external mixing. The problem is an important in the aerosol mixing study, but dealing with that problem in this paper seems to be able to get out of the subject of this study. For this reason, the expression that could cause controversy was deleted.

- I strongly suggest to specify the wavelength when the depolarization from AERONET and from

lidar is compared. For example, in page 28 line 594-595, the strongest correlation occurs between 1020 (AERONET) and 532(lidar) nm. This clarification is even more important in the summary/conclusion section since someone may directly read this section without paying attention to the rest of the manuscript, leading to misunderstandings. Page 29 line 618 is another example.

: As reviewer commented, specifying of the wavelength at 1020 nm was added in the summary/conclusion section.

Minor comments:

- Page 4 line 90: lidar.The → lidar. The

- Page 10 line 212: the particle linear depolarization ratio can be defined in different ways either perpendicular/parallel or perpendicular/total. I suggest to include a comment saying that both ways are interchangeable with a simple equation (Cairo, 1999).

: As reviewer suggested, the sentence has been added to explain about interchangeable of the linear volume depolarization ratio in line 235 - 239.

"A different definition of the δ^L ($\delta^{LT} = P_\perp/(P_\parallel + P_\perp)$) is used in many other studies, e.g., Noh et al. (2016; 2013b) and Sakai et al. (2000). The term δ^{LT} is defined differently from the definition we use for δ^L in our work. It is expressed by the following equation, derived from Eq. (3), see Cairo et al. (1999).

$$\delta^{LT} = \frac{\delta^L}{\delta^L + 1} \qquad (4)"$$

- Page 11 line 217: the same value of molecular depolarization means that the FWMH of the interference filter is the same one in all the lidars. Please, confirm.

: The same interference filters were used for each lidar system. And molecular depolarization ratio was not 0.0044 but 0.014. The related sentences have been added in the revised manuscript.

- Page 11 line 223: did the author try to use the backscatter ratio instead of the backscatter? Might it be produce the same result?

:The aerosol backscatter coefficient was used to calculate the weight factor. Also, if we used the backscatter ratio, the result must be the same with using of backscatter coefficient because only the ratio was applied in the calculation.

- Page 13 line 262: missed space between the symbol and the 'at'.

: It has been corrected in the revised manuscript.

- Page 13 line 273-274: the sentence indicates ‘cases with high δ’ but is written ‘(<0.25)’. Should it be (>0.25)? Or $0.1<\delta<0.25$?

:It was typo. It has been corrected as >0.25 in the revised manuscript.

- Page 27 line 580: I think that ‘from 2.85 to 1.85 μm between group 1 and group 6’ is enough.

: It has been corrected in the revised manuscript.

We responded to all the comments by the reviewer. The criticism and suggestions by the reviewer were appropriate and improved the quality of our manuscript. We appreciate such efforts.

Authors′ response to reviewers′ comments

Paper No.: acp-2016-1181
Title: **Depolarization Ratios Retrieved by AERONET Sun/Sky Radiometer Data and Comparison to Depolarization Ratios Measured With Lidar**

Revision of the paper

Reviewer #3

General comments:
The manuscript describes the results of comparing aerosol column value of particle linear backscatter depolarization ratio retrieved from AERONET sun-radiometer measurements, δ_P^S, and its direct measurements by lidar, δ_P^{CL}, as well as detailed analysis of the relationship between the parameter δ_P^S and the characteristics of the aerosol dust fraction. The results of this work can be implemented in observations of Asian dust transport.
Evaluation of aerosol depolarization ratio, δ_P^S, from AERONET measurements of direct and scattered solar radiation is the result of solving of "ill-posed" inverse problem. Correlation coefficients between δ_P^S and δ_P^{CL} characterize the uncertainties of parameter δ_P^S. It is useful information to improve the algorithms for processing data of complex experiments with employment of sun-radiometers and lidars.
I consider this paper to be a good and useful work and suggest to public it with some corrections.

Specific comments:
1. 1. The term "linear backscatter depolarization ratio" is used in the scientific literature to denote two similar but not identical parameters: the ratio of the backscatter perpendicular intensity to the parallel intensity, as well as the ratio perpendicular to the total backscattering intensity. The relationship between these quantities is nonlinear and for large depolarization the difference between parameters is significant. Therefore, at the beginning of this manuscript (in Abstract) it should be specified which parameters are used for characterization of radiometric and lidar data.

: We used the same physical meaning (the backscatter perpendicular intensity to the parallel intensity) in the data retrieval. The depolarization ratio by lidar measurement is also calculated by a meaning of $\frac{\beta_{P,\perp}}{\beta_{P,11}}$. The previous expression of $\delta^L(z) = \frac{P_\perp(z)}{P_{||}(z) + P_\perp(z)}$ is changed as $\delta^L(z) = \frac{P_\perp(z)}{P_{||}(z)}$ in the revised manuscript.

2. The question of the causes of the differences in depolarization evaluations, made from the results of radiometric and lidar measurements, is of interest. What part of these differences is caused by instrumental measurement errors?

: The lidar measured depolarization ratio is directly measured by backscatter signal. But, depolarization ratio retrieved by AERONET sun/sky radiometer measurement is the result of solving of "ill-posed inverse problem" as reviewer commented. Although the lidar measured depolarization ratio has systematic errors, the value is closed to real value. But, AERONET sun/sky radiometer data has not been verified yet. In that reason, we try to verify the reliability of AERONET-derived depolarization ratio by comparing lidar data.

AERONET-derived depolarization ratio at 1020 nm shows high correlation with lidar-derived depolarization ratio at 532 nm. But, AERONET-derived depolarization ratio at 440 nm shows low correlation. The explanation for the reason of these differences between AERONET-derived depolarization ratio at 440 nm and lidar –derived depolarization ratio at 532 nm has been newly added in the revised manuscript in line 325 - 388.

"We tried to find the reason for the comparably low correlation at 440 nm. For that reason, we retrieved the δ_P^S at 532 nm by interpolating the value of δ_P^S at 532 nm on the basis of the four AERONET wavelengths. In the next step the differences between δ_P^S and δ_P^{CL} at 532 nm ($\delta_{P\ 532}^{CL} - \delta_{P\ 532}^{S}$) were calculated by deducting δ_P^{CL} (at 532 nm) from δ_P^S (at 532 nm) for all 580 cases for which we have δ_P^S at the four AERONET sites.

The values $\delta_{P\ 532}^{CL} - \delta_{P\ 532}^{S}$ of were varied from 0.14 to -0.09. In the following step the data were sorted according to the differences of $\delta_{P\ 532}^{CL} - \delta_{P\ 532}^{S}$. In the final step we divided these differences into intervals of 0.02, i.e. 1: >0.12, 2: 0.10 - 0.12, 3: 0.08 - 0.10, …, 11: -0.06 – (-0.08), 12: <(-0.08).

Figure 5 shows the variation of the averaged δ_P^S at the five wavelengths and the values of δ_P^{CL} at 532 nm divided by the differences of $\delta_{P\ 532}^{CL} - \delta_{P\ 532}^{S}$. The differences of δ_P^S between the wavelengths at 440 nm and 1020 nm are high.

We find that decreasing of δ_P^S with increasing wavelength if the value of $\delta_{P\ 532}^{CL} - \delta_{P\ 532}^{S}$ is low. The differences between δ_P^S at 440 nm and δ_P^S at 1020 nm become less for increasing interval number, i.e. $\delta_{P\ 532}^{CL} - \delta_{P\ 532}^{S}$ for the interval number 7 (0 - 0.02); i.e. the yellow triangle pointing to the right . The value of δ_P^{CL} at 532 nm shows lower values than δ_P^S at 1020 nm in those intervals.

The differences between δ_P^{CL} at 532 nm and δ_P^{S} at 1020 nm are reduced as the $\delta_{P\ 532}^{CL} - \delta_{P\ 532}^{S}$ is decreased up to the interval number 7 (0-0.02). We find an increasing of δ_P^{S} with increasing wavelength from the interval number 8 (0-(-0.02)) . The value of δ_P^{CL} at 532 nm is larger than the value of δ_P^{S} at 1020 nm in the interval number 8 (0-(-0.02)). Also, the differences between δ_P^{CL} at 532 nm and δ_P^{S} at 1020 nm as the interval number increased..

If we assume that the value of δ_P^{CL} at 532 nm is close to real value of δ_P, the results in Figure 5 indicate that the δ_P^{S} at 440 nm has been retrieved to be higher value than the δ_P^{CL} at 532 nm in the interval number from 1 (>0.12) to 7 (0-0.02) when the δ_P^{CL} at 532 nm showed low values (less than 0.08). Conversely, when the high δ_P^{CL} at 532 nm was measured, the δ_P^{S} at 440 nm showed a lower value than the δ_P^{CL} at 532 nm.

Figure 6 shows the average of volume particle size distributions of each interval data as separated in Figure 5. We see that the volume size distributions change from fine-mode dominated size distributions to coarse-mode dominated size distributions when the interval number moves from 1 (>0.12) to 12 (<(-0.08)).

The important point of Figure 6 is the variation of the volume median radius (Rv). The volume median radius of the coarse (Rv_c) and the fine (Rv_f) mode shows a maximum value at the interval number 1 (>0.12). Rv_f clearly and progressively decreases as the interval number moves from 1 (>0.12) to 12 (<(-0.08)). The Rv_f of the interval number 1 (>0.12) is two time larger than the interval number of 12 (<(-0.08)) as 0.28 ± 0.03 μm and 0.13 ± 0.01 μm, respectively. Rv_c also shows a pattern of decreasing values with decreasing values of $\delta_{P\ 532}^{CL} - \delta_{P\ 532}^{S}$. But it does not show as progressively as Rv_f.

Figures 5 and 6 show that the value of δ_P^{S} at 440 nm tends to be retrieved high for conditions where there is no dust at all or the dust concentration is low. Such conditions are usually dominated by a significant fine-mode of the particle size distribution.

When dust particles contribute the main share to the particle concentration, i.e. high values of δ_P^{CL} at 532 nm, the contribution of fine-mode particles is small. When particles in the fine-mode are the main contribution of the particle size distribution, i.e. low values of δ_P^{CL} at 532 nm, the size of the particles in the fine-mode fraction are considered to have a large influence on the retrieval of the values of δ_P^{S}. This effect is considered to be more significant at 440 nm, i.e. at short wavelengths.

Mamouri and Ansmann (2017) found that the value of δ_P^{L} is maximum at 532 nm and lower at 355

and 1064 nm because of the competing influence the fine-mode and coarse-mode dust fraction have on the overall values (fine + coarse) of δ_P^L at the three wavelengths.

Haarig et al. (2017) found that on average the values of δ_P^L for aged Saharan dust were 0.25 at 355 nm, 0.31 at 532 nm, and 0.225 at 1064 nm. Müller et al. (2010; 2012) and Freudenthaler et al. (2009) also found spectral slope of the depolarization ratio with the maximum at 532 nm and lower values at 355 and 1064 nm during the Saharan Mineral Dust Experiment (SAMUM) 2006. The results clearly show a different pattern of the spectral variations of δ_P measured by lidar and retrieved from Sun/sky radiometer observations of dust.

It is a striking result that δ_P^S at 1020 nm, unlike δ_P^S at 440 nm, is very similar to the values of δ_P^{CL} at 532 nm. Though we cannot identify the reason for this similarity and even if the wavelengths (lidar at 532 nm and AERONET Sun/sky radiometer at 1020 nm) are different we may use the values of δ_P^S at 1020 nm as a qualitative indicator of the presence of mineral dust particles in the atmosphere. It remains open if we can use this parameter also as a qualitative measure of the mixing ratio of mineral dust and anthropogenic pollution particles compared to the more robust parameter δ_P^{CL} (at 532 nm)."

3. Line 217: "The molecular depolarization ratio is assumed to be 0.0044". It means that all lidar systems have optical filters with very small bandwidth and measure almost only central Cabannes line of Rayleigh scattering (PC-SCI-201, CALIOP Algorithm Theoretical Basis Document Calibration and Level 1 Data Products).

: The same interference filters were used to each lidar system. And molecular depolarization ratio was not 0.0044 but 0.014. The related sentences have been added in the revised manuscript.

4. Lines 41-44 in Abstract (the same, in Summary) should be compared to lines 362 -363.

: The long word "decreasing" has been corrected as "increase" in Abstract and summary in the revised manuscript.

Depolarization Ratios Retrieved by AERONET Sun/sky Radiometer Data and Comparison to Depolarization Ratios Measured With Lidar

Youngmin Noh[1], Detlef Müller[2*], Kyunghwa Lee[3], Kwanchul Kim[3], Kwonho Lee[4], Atsushi Shimizu[5]

[1] International Environmental Research Center, Gwangju Institute of Science and Technology (GIST), Korea

[2] University of Hertfordshire, United Kingdom

[3] Gwangju Institute of Science and Technology (GIST), Korea

[4] Gangneung-Wonju National University, Korea

[5] National Institute for Environmental Studies, Japan

29 December 2016

[*]Corresponding Author:

School of Physics, Astronomy and Mathematics, University of Hertfordshire, Hertfordshire, UK

Tel: +44-1707-28-4365

E-mail address: d.mueller@herts.ac.uk (Detlef Müller)

Abstract

The linear particle depolarization ratios at 440, 675, 870, and 1020 nm were derived using data taken with AERONET Sun/sky radiometer at Seoul (37.45° N, 126.95° E), Kongju (36.47° N, 127.14° E), Gosan (33.29° N, 126.16° E), and Osaka (34.65° N, 135.59° E). The results are compared to the linear particle depolarization ratio measured by lidar at 532 nm. The correlation coefficient R^2 between the linear particle depolarization ratio derived by AERONET data at 1020 nm and the linear particle depolarization ratio measured with lidar at 532 nm is 0.90, 0.92, 0.79, and 0.89 at Seoul, Kongju, Gosan, and Osaka, respectively. The correlation coefficients between the lidar-measured depolarization ratio at 532 nm and the one retrieved by AERONET at 870 nm are 0.89, 0.92, 0.76, and 0.88 at Seoul, Kongju, Gosan, and Osaka, respectively. The correlation coefficients for the data taken at 675 nm are lower than the correlation coefficients at 870 and 1020 nm, respectively. Values are 0.81, 0.90, 0.64, and 0.81 at Seoul, Kongju, Gosan, and Osaka, respectively. The lowest correlation values are found for the AERONET-derived linear particle depolarization ratio at 440 nm, i.e. 0.38, 0.62, 0.26, and 0.28 at Seoul, Kongju, Gosan, and Osaka, respectively. We should expect a higher correlation between lidar-measured linear particle depolarization ratios at 532 nm and the ones derived from AERONET at 675 nm and 440 nm as the lidar wavelength is between the two AERONET wavelengths. We cannot explain at the moment we find better correlation between lidar and AERONET linear particle depolarization ratios for the case that the AERONET wavelengths are significantly larger than the lidar measurement wavelength.

The linear particle depolarization ratio can be used as a parameter to obtain insight into the variation of optical and microphysical properties of dust when it is mixed with anthropogenic pollution particles. The single-scattering albedo increases with increasing measurement

wavelength for low linear particle depolarization ratios, which indicates a high share of fine-mode anthropogenic pollution. In contrast, single-scattering albedo increases with increasing wavelength for high linear particle depolarization ratios, which indicated a high share of coarse-mode mineral dust particles. The retrieved volume particle size distributions are dominated by the fine-mode fraction if linear particle depolarization ratios are less than 0.15 at 532 nm. The fine-mode fraction of the size distributions decreases and the coarse-mode fraction of the size distribution increases for increasing linear particle depolarization ratio at 1020 nm. The dust ratio based on using the linear particle depolarization ratio derived from AERONET data is 0.12 to 0.17. These values are lower than the coarse-mode fraction derived from the volume concentrations of particle size distributions in which case we can compute the coarse-mode fraction of dust.

Key words: linear particle depolarization ratio, lidar, AERONET Sun/sky radiometer, dust, single-scattering albedo, size distribution

1. Introduction

There are various aerosol types of natural (primarily desert dust and sea salt) and anthropogenic (primarily combustion of biomass and fossil fuels) origin. A precise understanding of the radiative forcing of these aerosol types is the key to quantifying the aerosol impact on regional and global climate change (IPCC, 2013). In order to better estimate the aerosol effect (direct and indirect radiative forcing) on global climate change many studies have been performed with the goal of classifying aerosol types (Burton et al., 2013; Eck et al., 2010; 1999; Lee et al., 2010a; Dubovik et al, 2002). However, those studies

do not separate aerosol types according to their contribution of mixed aerosols (respectively mixtures of different aerosol types) in a plume, but merely classify dominant aerosol types based on the optical properties of aerosols.

Dust is one of the major aerosol components in the atmosphere. Dust affects Earth's climate by interacting with solar as well as thermal infrared radiation. Dust also affects atmospheric dynamics, atmospheric chemistry, air quality, and ocean biogeochemistry over a wide range of spatial and temporal scales, e.g., Haywood et al. (2005), Jickells et al. (2005) and Husar et al. (2001). On the global average, dust contributes to about one quarter of aerosol optical depth (τ) in the mid-visible wavelength range (Kinne et al., 2006). Dust is also light-absorbing (Lafon et al., 2006 and 2004; Alfaro et al., 2004; Sokolik and Toon, 1999). It is estimated that more than half of aerosol absorption optical depth at 550 nm may come from dust (Chin et al., 2009).

The size distribution and absorption properties of desert dust and anthropogenic aerosols show properties that can be clearly distinguished (Russel et al., 2010; Dubovik et al., 2002). Desert dust predominately consists of coarse mode particles (typical radius > ~1 μm). In contrast, combustion-produced particles are predominately found in the fine-mode fraction of particle size distributions (typically radius < ~1 μm). Aerosols in which fractions of fine-mode and coarse-mode particles are mixed are among the most challenging aerosol types to characterize. If we can separate desert dust from other aerosols in mixed dust plumes, we will improve our understanding of the effect those mixed aerosol plumes have on climate change.

The linear particle depolarization ratio (δ_p) strongly depends on particle shape. Since dust particles have non-spherical shape, the δ_p can be used to identify the presence of dust particles in the atmosphere. In that regard lidar is a particularly powerful measurement

technique (Shimizu et al., 2017; Tesche et al., 2009; Noh et al., 2008; 2007; Iwasaka et al., 2003; Cairo et al., 1999). The δ_p has also been used to identify biogenic aerosols. Noh et al. (2013a,b) and Sassen et al. (2008) identified the vertical distribution of pollen in the atmosphere using the δ_p measured by lidar. The possibility that dust particles are mixed with other, man-made pollution and/or biomass burning particles is very high, except in source regions of dust emissions where population density, and thus emissions caused by human activities are comparably low (Sun et al., 2010; 2005; Yu et al., 2006). Mixtures of dust particles and anthropogenic particles cause changes in the δ_p of dust plumes. Shin et al. (2015) reported on lidar measurements and show that the δ_p decreases when dust is mixed with pollution particles. The δ_p is also a very useful parameter that allows us to separate dust from non-dust particles (anthropogenic, smoke, and sulphate particles) in mixed dust plumes by retrieving the dust ratio (R_D). Shimizu et al. (2004) estimated the contributions of dust and pollution particles in a mixed-dust plume by the assumption that both aerosol types are externally mixed. The optical data of these mixed dust plumes were separated by the R_D into pure dust content and the contribution by anthropogenic particles (Noh et al., 2016a; Bravo-Aranda et al., 2015; Noh 2014; Noh et al., 2012b;). Tesche et al. (2011) separated the optical properties of desert dust and biomass burning particles in mixed dust and smoke plumes observed over the tropical North Atlantic, west of the African continent. The authors used multi-wavelength aerosol Raman lidar in combination with polarization lidar. Burton et al. (2014) provides a generalized version of the separation methodology between two aerosol types, i.e. urban pollution plus dust, marine plus dust, and smoke plus marine by modifying the methodology suggested by Shimizu et al. (2004) and Tesche et al. (2011). Noh (2014) and

Tesche et al. (2011; 2009) used the δ_p to retrieve vertically-resolved single-scattering albedo of mixed dust plumes by separating the contribution of dust and non-dust particles. Ansmann et al. (2011) and Navas-Guzmán et al. (2013) separated the contribution of volcanic ash and sulphate particles to total backscatter and extinction coefficient by using the δ_p.

However, the number of lidar measurement sites is limited and provides rather sparse spatially-resolved and temporally-resolved information on the global scale. Thus, we need another methods that could allow us to measure δ_p.

AERONET (Aerosol Robotic NETwork) is an automated, robotic Sun-and-sky-scanning measurement network that took respectively still collects data at more than 797 measurement sites worldwide (http://aeronet.gsfc.nasa.gov/). These sites span everything from temporally limited observations at sites at which field campaigns were carried out to sites that carry out long-term observations since AERONET started with its observations. AERONET Sun/sky radiometers provide globally distributed observations of spectrally-resolved aerosol optical depth (τ) and data inversion products such as particle size distributions and complex refractive indices of different aerosol types (Holben et al., 1998).

Dubovik et al. (2006) suggested to use AERONET Sun/sky radiometer data to retrieve δ_p.

Müller et al. (2012; 2010) calculated the δ_p of Saharan dust using AERONET Sun/sky radiometer data. Noh et al. (2016b) and Lee et al. (2010b) used AERONET Sun/sky radiometer data to retrieve the δ_p of Asian dust. However, only cases of nearly pure desert-dust particle were analyzed in these studies. There exist no studies in which the δ_p for various mixtures (mixing ratio) between desert dust and anthropogenic pollution particles using AERONET data has been determined.

In this contribution we attempt to verify the reliability of AERONET-derived values of δ_p by comparing these values to values of δ_p measured by lidar.

Section 2 presents the methods used in this study. Section 3 presents our results. We discuss our results and summarize our findings in section 4.

2. Methodology

2.1 Study sites

The AERONET sites considered in this study are all located along the pathway of the regime of prevailing westerly winds that serve as major transport routes of Asian dust which is advected from the arid regions of China and Mongolia. Figure 1 shows the locations of the AERONET Sun/sky radiometers and lidars used in this study.

Seoul (37.45°N, 126.95° E) and Kongju (36.47° N, 127.14° E) are located inland (continental influenced), whereas Gosan (33.29°N, 126.16° E) and Osaka (34.65° N, 135.59° E) are coastal sites. The Gosan site faces the Yellow Sea and is considered an ideal location for monitoring regional background aerosols in East Asia because there are few local industrial sources in that region. The other three sites are located inside large cities. We also use data from the AERONET site at Dunhuang (40.49° N, 94.95° E) in our study, and we analyzed the depolarization ratios and optical properties of pure Asian dust at this source region.

Lidar data are obtained from the lidar network of the National Institute of Environmental Research (NIES), Japan. The lidars operated in this network are two-wavelength (1064

nm and 532 nm) Mie-scattering lidars that also measure the linear particle depolarization ratio at 532 nm. The details of these lidar systems and data processing procedures are explained by Shimizu et al. (2017) and Sugimoto et al. (2014).

The locations of the lidar systems used for our research work are the same as the locations of the AERONET systems for the sites in Seoul, Gosan, and Osaka. The lidar used for the Kongju site is located approximately 32 km away to Northwest direction from the AERONET site.

2.2 Depolarization ratios derived from data taken with AERONET Sun/sky radiometer

Dubovik et al. (2006) introduced kernel look-up tables that describe mixtures of spheroid particles. These kernel look-up tables were used to infer the δ_p of mineral dust observed with Sun/sky radiometer. The details of the AERONET inversion algorithm that processes data of mineral dust are given by Dubovik et al. (2006).

Briefly, the retrieval of the depolarization ratios works as follows. The elements $F_{11}(\lambda)$ and $F_{22}(\lambda)$ of the Müller scattering matrices (Bohren and Huffman, 1983) are computed from the retrieved complex refractive indices and particle size distributions. The term $F_{11}(\lambda)$ is proportional to the flux of the scattered light (Volten et al., 2001) in the case of unpolarized incident light,. The $F_{22}(\lambda)$-term in turn follows from the angular and spectral distribution of the radiative intensity which is measured with the AERONET instrument (Dubovik et al., 2006). Another input parameter that is needed for the retrieval of δ_p is the aspect-ratio distribution. The aspect ratio indicates the ratio of a particle's longest axis to its shortest axis. In the case of prolate particles its polar diameter is greater than the equatorial

diameter, in contrast to oblate particles where this ratio is vice versa. The aspect ratio distribution is kept to a fixed distribution in the AERONET model since scattering elements are nearly equivalent for all mixtures of spheroid particles (Dubovik et al., 2006).

From the ratio of the elements $F_{11}(\lambda)$ and $F_{22}(\lambda)$ at the scattering angle 180° the $\delta_p(\lambda)$ can be computed as

$$\delta_p(\lambda) = \frac{1 - F_{22}(\lambda, 180°) / F_{11}(\lambda, 180°)}{1 + F_{22}(\lambda, 180°) / F_{11}(\lambda, 180°)} \qquad (1)$$

The δ_P derived from the Sun/sky radiometer data is written as δ_P^S so that we can distinguish it from the lidar-derived δ_P, i.e. δ_P^L.

The contributions of dust and anthropogenic pollution particles to the total backscatter coefficients of mixed aerosol plumes were estimated from the δ_P under the assumption that both types of aerosol particles are externally mixed. The dust ratio (R_D) of the dust-related backscatter coefficient to the total backscatter coefficient was calculated using Eq. (1), based on the method suggested by Shimizu et al. (2004):

$$R_D = \frac{(\delta_P^S - \delta_2)(1 + \delta_1)}{(\delta_1 - \delta_2)(1 + \delta_P^S)} \qquad (2)$$

where δ_1 and δ_2 denote the δ_P^S of pure dust and non-dust particles (i.e. the total aerosol plume without the contribution by dust), respectively, in the external mixture of aerosol particles. The values δ_1 and δ_2 can be empirically determined. In the present study, we used the value 0.34 for δ_1. This value was derived from adding 0.01 to the maximum value observed at the Dunhuang site (Asian dust source region). The value of 0.02 was used for δ_2,

which is the minimum value used in this study. When δ_P^S was higher than δ_1 or lower than δ_2, R_D was set to 1 or 0, respectively.

Two kinds of coarse-mode fractions (CMF) were calculated. The coarse-mode fraction of the aerosol optical depth (τ) (CMFτ) is calculated from the ratio of the coarse-mode τ to the total (coarse + fine mode) τ at the same wavelength at which the δ_P^S is available. The coarse-mode fraction is also calculated on the basis of the volume concentration (CMF_{vc}).

2.3 Column-integrated depolarization ratio measured by LIDAR

The lidar systems used in our study measure the linear volume depolarization ratio (aerosols + molecules; δ^L) from the linearly- and perpendicularly-polarized components of the Mie/Rayleigh backscatter signals at 532 nm wavelength (Shimizu et al., 2004). The value of δ^L is defined as

$$\delta^L(z) = \frac{P_\perp(z)}{P_\parallel(z)} \tag{3}$$

where P(z) is the backscatter signal with respect to height z. The symbols $\parallel$ and $\perp$ denote the linearl-y and perpendicularly-polarized components with respect to the plane of polarization of the emitted laser light, respectively.

In order to obtain reliable depolarization ratios, the data of the lidar measurements must be calibrated before physical quantities such as the linear volume depolarization ratio can be retrieved. It is important to calibrate the signal intensities of the $P_\parallel$ and $P_\perp$ first, before the

linear volume depolarization ratio is calculated. Thet calibration method of the lidar system is explained in detail by Shimizu et al. (2017) and Nishizawa et al. (2017).

The difference of the sensitivity between two PMTs that are used by the lidar system to detect these components is checked regularly by the following method. A sheet polarizer whose polarizing direction is set at 45° to the polarizing plane of the emitted light is inserted in front of the beam splitter cube, and the backscatter signal from the sky is recorded as a reference signal. In this reference record, the light intensities of the two channels are equal after the sheet polarizer, so the calibration constant can be obtained by comparing the recorded values of $P_{\parallel}$ and $P_{\perp}$. In the next step, the sheet polarizer is rotated by 90° which sets the polarizing angle at −45°, and another reference signal is recorded. Then relative calibration of $P_{\parallel}$ and $P_{\perp}$ channels using signals measured for the polarizing angles at ± 45°. This pair of reference signals reduces any error caused by a poor positioning of the sheet polarizer (Freudenthaler et al., 2009; 2016). The reference signals are usually recorded once per year for each lidar (Shimizu et al., 2017).

A different definition of the δ^{L} ($\delta^{LT} = P_{\square}/(P_{\parallel} + P_{\square})$) is used in many other studies, e.g., Noh et al. (2016; 2013b) and Sakai et al. (2000). The term δ^{LT} is defined differently from the definition we use for δ^{L} in our work. It is expressed by the following equation, derived from Eq. (3), see Cairo et al. (1999).

$$\delta^{LT} = \frac{\delta^{L}}{\delta^{L} + 1} \tag{4}$$

The variable δ_P^L differs from δ^L as it depends on the concentration of particles and it does not take account of the contribution (concentration) of air molecules. In this contribution, δ_P^L can be calculated on the basis of the definition provided by Sakai et al. (2000)

$$\delta_P^L(z) = \frac{\delta^L(z)(R(z) + R(z) \times \delta_M - \delta_M) - \delta_M}{R(z) - 1 + R(z) \times \delta_M - \delta^L(z)} (\%) . \quad (5)$$

The backscatter ratio R is the ratio of the sum of the aerosol backscatter coefficient ($\beta_P + \beta_M$) to the pure molecular backscatter coefficient (β_M), which, according to Whiteman et al. (1992) can be expressed by

$$R(z) = \frac{\beta_P(z) + \beta_M(z)}{\beta_M(z)} \quad (6)$$

β_P and β_M are the volume backscatter coefficients of aerosol particles and air molecules, respectively. The molecular depolarization ratio (δ_M) is assumed to be 0.014 (Shimizu et al., 2004).

The parameter δ_P^L can be derived by lidar measurements in terms of vertical profiles. In contrast, δ_P^S describes a column-integrated value. For that reason, δ_P^L had to be changed to column-integrated values in our study so that we could carry out a direct comparison with δ_P^S.

The column-integrated and weighted values of δ_P^L (δ_P^{CL}) can be calculated by

$$\delta_P^{CL} = \int_0^z \delta_P^L(z) W(z) dz \quad (7)$$

where the term W(z) is a weight factor that is calculated by using the measured aerosol backscatter coefficient (β_P) according to

$$W(z) = \frac{\beta_P(z)}{\int_0^z \beta_P(z)dz} \tag{8}$$

The aerosol backscatter coefficient is derived by the backward version of Fernald's method (Fernald, 1984). The data observed at 9 km height are used as reference height for the analysis of data taken under cloud-free conditions.

The reference height is lowered if the signal-to-noise ratio at 9 km is not sufficient which may be the case of high aerosol concentration. Molecular density profiles are taken from the COSPAR international reference atmosphere (CIRA-86) for computing the Rayleigh scattering component. A constant lidar ratio of 50 sr is applied in the calculation of the aerosol backscatter coefficients (Shimizu et al., 2017). Since the lidar ratio differs for different aerosol types, the selection of the lidar ratio is important to obtain exact values of extinction and backscatter coefficients. However, we only use the ratio of the backscatter coefficient in the calculation of W(z) in our study. For that reason, the value of the lidar ratio does not affect the calculation of W(z).

Figure 2 shows a retrieval example of δ_P^{CL}. Three cases, corresponding to lidar measurements carried out at 23:00 UTC (start time of measurement) on 13 March 2010 (a), at 06:00 UTC on 22 March 2010 (b), and at 23:15 on 3 May 2010 (c) are shown. The measurement on 13 March 2010 describes an aerosol plume that has a high value of δ_P^L and a high value of β_P (case 1, Fig. 2 (a)). The measurement on 22 March 2010 describes an aerosol plume with high β_P below and above the planetary boundary layer (PBL), respectively. However, a high value of δ_P^L is detected above the PBL (case 2, Fig. 2 (b))

only. The measurement on 2 May 2010 describes an aerosol plume with low backscatter coefficients and a high value of δ_P^L (case 3, Fig. 2 (c)). The averaged values of δ_P^L (δ_{ave}) which do not consider the backscatter intensity but just the averaged δ_P^L from the bottom to the top height of the profiles of δ_P^L are listed in Figure 2, too.

The values of δ_P^S at 1020 nm are 0.250, 0.140, and 0.164 for the cases 1, 2, and 3, respectively. The values of δ_P^{CL} are similar to the values of δ_P^S. We find 0.243, 0.129, and 0.157 for the cases 1, 2, and 3, respectively. However, the values of δ_{ave} for case 1 and case 3 are different compared to the values of δ_P^S. Since δ_P^L is not directly related to aerosol concentration but only to the non-sphericity of (an ensemble of) aerosol particles (inside a given volume of air) large values of δ_P^L can occur for high as well as for low aerosol backscatter coefficients. Lower values of δ_{ave} compared to δ_P^S are linked to high values of δ_P^L for the case of high aerosol backscatter coefficients of a thin aerosol layer, see Figure 2 (a). We find that the value of δ_{ave} is higher than the value of δ_P^S for the situation in which a high value of δ_P^L is combined with a low aerosol backscatter coefficient, see Figure 2 (3)). The examples in Figure 2 show that δ_P^{CL} has to be compared with δ_P^S.

3. Results and Discussion

3. 1. AERONET-derived depolarization ratios and lidar-measured values: comparison

Figure 3 shows the temporal variation of τ at 500 nm and the values of δ_P^S at 1020 nm at the four AERONET sites. The combined data of the four sites are shown in the same figure. The number of measurement cases for the four sites are listed in Table 1. The total number of

retrieved values of δ_P^S is 163, 44, 139, and 234 at Seoul, Kongju, Gosan, and Osaka, respectively. Since the measurement cases are limited it is difficult to analyze seasonal trends. However, we find high values of τ and δ_P^S in spring (March to May). We assume that these high values are caused by transport of dust from East Asia to the Pacific Ocean.

Figure 4 presents scatterplots of δ_P^{CL} and δ_P^S at the four AERONET sites. We compare the values of the δ_P^S at these four wavelengths (440, 675, 870, and 1020 nm) to the values of δ_P^{CL} at 532 nm. The correlation coefficients R^2 at 1020 nm are high. We find 0.90, 0.92, 0.79, and 0.89 at Seoul, Kongju, Gosan, and Osaka, respectively.

We find similarly high correlation between δ_P^{CL} and δ_P^S at 870 nm, i.e. numbers are 0.89, 0.92, 0.76, and 0.88 at Seoul, Kongju, Gosan, and Osaka, respectively. The correlation at 675 nm is lower compared to the values we find at 870 and 1020 nm. Values are 0.81, 0.90, 0.64, and 0.81 at Seoul, Kongju, Gosan, and Osaka, respectively. The correlation is significantly low at 440 nm. Values are 0.38, 0.62, 0.26, and 0.28 at Seoul, Kongju, Gosan, and Osaka, respectively.

The correlation coefficient at 440 nm at Kongju is much higher than at the other sites. This higher correlation may be caused by the limited number of observational data and/or observation times. Only 44 cases were taken during a short period of two months, from April to May 2012 at Kongju.

Figure 4 shows that the differences between δ_P^{CL} and δ_P^S are high when the value of δ_P^{CL} is less than 0.10 at Seoul, Gosan and Osaka. However, the number of cases of low δ_P^{CL} (< 0.10) is comparably low at Kongju compared to the other sites. The number of cases with high δ_P^{CL} (> 0.25) is comparably high (with respect to all cases), i.e. 23% (10 cases out of

44 in total), compared to what we find for the other sites: 0/163, 3/139, and 10/234 at Seoul, Gosan, and Osaka, respectively (see Table 1).

We tried to find the reason for the comparably low correlation at 440 nm. For that reason, we retrieved the δ_P^S at 532 nm by interpolating the value of δ_P^S at 532 nm on the basis of the four AERONET wavelengths. In the next step the differences between δ_P^S and δ_P^{CL} at 532 nm ($\delta_{P\ 532}^{CL} - \delta_{P\ 532}^{S}$) were calculated by deducting δ_P^{CL} (at 532 nm) from δ_P^S (at 532 nm) for all 580 cases for which we have δ_P^S at the four AERONET sites.

The values $\delta_{P\ 532}^{CL} - \delta_{P\ 532}^{S}$ of were varied from 0.14 to -0.09. In the following step the data were sorted according to the differences of $\delta_{P\ 532}^{CL} - \delta_{P\ 532}^{S}$. In the final step we divided these differences into intervals of 0.02, i.e. 1: >0.12, 2: 0.10 - 0.12, 3: 0.08 - 0.10, …, 11: -0.06 – (-0.08), 12: <(-0.08).

Figure 5 shows the variation of the averaged δ_P^S at the five wavelengths and the values of δ_P^{CL} at 532 nm divided by the differences of $\delta_{P\ 532}^{CL} - \delta_{P\ 532}^{S}$. The differences of δ_P^S between the wavelengths at 440 nm and 1020 nm are high.

We find that decreasing of δ_P^S with increasing wavelength if the value of $\delta_{P\ 532}^{CL} - \delta_{P\ 532}^{S}$ is low. The differences between δ_P^S at 440 nm and δ_P^S at 1020 nm become less for increasing interval number, i.e. $\delta_{P\ 532}^{CL} - \delta_{P\ 532}^{S}$ for the interval number 7 (0 - 0.02); i.e. the yellow triangle pointing to the right . The value of δ_P^{CL} at 532 nm shows lower values than δ_P^S at 1020 nm in those intervals. The differences between δ_P^{CL} at 532 nm and δ_P^S at 1020 nm are reduced as the $\delta_{P\ 532}^{CL} - \delta_{P\ 532}^{S}$ is decreased up to the interval number 7 (0-0.02). We find an

increasing of δ_P^S with increasing wavelength from the interval number 8 (0-(-0.02)) . The value of δ_P^{CL} at 532 nm is larger than the value of δ_P^S at 1020 nm in the interval number 8 (0-(-0.02)). Also, the differences between δ_P^{CL} at 532 nm and δ_P^S at 1020 nm as the interval number increased..

If we assume that the value of δ_P^{CL} at 532 nm is close to real value of δ_P, the results in Figure 5 indicate that the δ_P^S at 440 nm has been retrieved to be higher value than the δ_P^{CL} at 532 nm in the interval number from 1 (>0.12) to 7 (0-0.02) when the δ_P^{CL} at 532 nm showed low values (less than 0.08). Conversely, when the high δ_P^{CL} at 532 nm was measured, the δ_P^S at 440 nm showed a lower value than the δ_P^{CL} at 532 nm.

Figure 6 shows the average of volume particle size distributions of each interval data as separated in Figure 5. We see that the volume size distributions change from fine-mode dominated size distributions to coarse-mode dominated size distributions when the interval number moves from 1 (>0.12) to 12 (<(-0.08)).

The important point of Figure 6 is the variation of the volume median radius (Rv). The volume median radius of the coarse (Rv_c) and the fine (Rv_f) mode shows a maximum value at the interval number 1 (>0.12). Rv_f clearly and progressively decreases as the interval number moves from 1 (>0.12) to 12 (<(-0.08)). The Rv_f of the interval number 1 (>0.12) is two time larger than the interval number of 12 (<(-0.08)) as 0.28 ± 0.03 μm and 0.13 ± 0.01 μm, respectively. Rv_c also shows a pattern of decreasing values with decreasing values of $\delta_{P\ 532}^{CL} - \delta_{P\ 532}^{S}$. But it does not show as progressively as Rv_f.

Figures 5 and 6 show that the value of δ_P^S at 440 nm tends to be retrieved high for

conditions where there is no dust at all or the dust concentration is low. Such conditions are usually dominated by a significant fine-mode of the particle size distribution.

When dust particles contribute the main share to the particle concentration, i.e. high values of δ_P^{CL} at 532 nm, the contribution of fine-mode particles is small. When particles in the fine-mode are the main contribution of the particle size distribution, i.e. low values of δ_P^{CL} at 532 nm, the size of the particles in the fine-mode fraction are considered to have a large influence on the retrieval of the values of δ_P^{S}. This effect is considered to be more significant at 440 nm, i.e. at short wavelengths.

Mamouri and Ansmann (2017) found that the value of δ_P^{L} is maximum at 532 nm and lower at 355 and 1064 nm because of the competing influence the fine-mode and coarse-mode dust fraction have on the overall values (fine + coarse) of δ_P^{L} at the three wavelengths.

Haarig et al. (2017) found that on average the values of δ_P^{L} for aged Saharan dust were 0.25 at 355 nm, 0.31 at 532 nm, and 0.225 at 1064 nm. Müller et al. (2010; 2012) and Freudenthaler et al. (2009) also found spectral slope of the depolarization ratio with the maximum at 532 nm and lower values at 355 and 1064 nm during the Saharan Mineral Dust Experiment (SAMUM) 2006. The results clearly show a different pattern of the spectral variations of δ_P measured by lidar and retrieved from Sun/sky radiometer observations of dust.

It is a striking result that δ_P^{S} at 1020 nm, unlike δ_P^{S} at 440 nm, is very similar to the values of δ_P^{CL} at 532 nm. Though we cannot identify the reason for this similarity and even if the wavelengths (lidar at 532 nm and AERONET Sun/sky radiometer at 1020 nm) are different we may use the values of δ_P^{S} at 1020 nm as a qualitative indicator of the presence of mineral

dust particles in the atmosphere. It remains open if we can use this parameter also as a qualitative measure of the mixing ratio of mineral dust and anthropogenic pollution particles compared to the more robust parameter δ_P^{CL} (at 532 nm).

3. 2. Classification of AERONET-derived depolarization ratios based on values of δ_P^S at 1020 nm.

The previous section showed that the depolarization ratio from AERONET does not a gree with the lidar values at 532 nm. A quantitative interpretation of the AERONET values is not possible. However, even if the quantitative numbers are wrong there ma y still be a possibility to use the AERONET numbers as qualitative indicators, i.e. tre nd. We must keep in mind, however, that the spectral slope of the depolarization rati os from AERONET are not correct for cases of (high) dust load.

We classified the observational data into 6 groups based on the values of δ_P^S at 1020 nm. Group 1 contains cases for which the values of δ_P^S are than 0.05 at 1020 nm. Groups 2, 3, 4, and 5 include values between 0.05 - 0.1, 0.1 - 0.15, 0.15 - 0.2, and 0.2 - 0.25 at 1020 nm, respectively. Values are above 0.25 in group 6.

Table 1 shows the number of data sets (observation cases) for each of the 6 data groups at the four observation sites. Table 1 also lists the averaged values of τ at 500 nm, the optical-depth-related Ångström exponent (å) between 440 and 870 nm, and the light-absorption-related Ångström exponent ($å_{A)}$ between 440 and 870 nm of each group. The values of τ are similar in all six groups. Reason for that similarity is because τ is insensitive to the shape and size of the particles. The values of $å_A$ increase. The values of å decrease with increasing value of δ_P^S.

Figure 7 shows the values δ_P^S of the six groups at the four measurement wavelengths of the AERONET Sun/sky radiometers. There is a rather clear increase of δ_P^S with respect to increasing measurement wavelength in group 6. We see a similar pattern in groups 4 and 5, respectively. In contrast, groups 1 - 3 show the highest values of δ_P^S at 440 nm whereas the values of δ_P^S are similar at the other three measurement wavelengths.

Values of δ_P^L of pure mineral dust plumes were measured at three wavelengths (355, 532, and 1064 nm) with lidar (Freudenthaler et al., 2009) during the Saharan Mineral Dust Experiment (SAMUM) in 2006. Freudenthaler et al. (2009) found values of 0.31 for δ_P^L at 532 nm. Müller et al. (2010; 2012) compared those data with data derived from collocated AERONET Sun/sky radiometer observations. Values of δ_p from both instruments agree at 1064-nm wavelength (Müller et al., 2010; 2012). If the Sun/sky radiometer results are extrapolated to the lidar wavelength of 355 nm, the value of δ_p obtained from the Sun/sky radiometer is 20 % lower than the value obtained from the lidar observations, see Figure 3 in Müller et al. (2010) and Figure 7 in Müller et al. (2012).

Müller et al. (2010) find that the values of δ_p inferred from the Sun/sky radiometer observations tend to be lower than the values measured with lidar for the case of pure mineral dust. Only group 6 (Kongju and Gosan) shows 20% - 30% lower values of δ_P^S compared to δ_P^{CL} in the visible wavelength range, which is a similar trend reported by Müller et al. (2010). This feature, i.e. that δ_P^{CL} is higher than δ_P^S is also found in group 5. However, the differences of the numbers are less compared to the differences we find for group 6. The opposite situation, i.e. δ_P^{CL} is lower than δ_P^S is found in groups 1, 2, and 3. Figure 4 ahows

that the value of δ_P^S at 440 nm are significantly different from the values found at the other three wavelengths.

Figure 7 shows the values of δ_P^{CL} at 532 nm of each group. We find 0.27 ± 0.02 and 0.27 ± 0.03 at Kongju and Gosan, respectively, for group 6. The values at the Osaka site are lower. We find 0.21 ± 0.04. The highest values of δ_P^{CL} are 0.29 at the Kongju and Gosan sites, respectively, see Figure 4.

The differences of the δ_p at the observation sites likely are caused by the appearance of dust. The transport distance to the four observation sites may have influence on the values of δ_p. Kongju and Gosan have similar transport distances from the source regions of East Asian dust. Osaka is located at a distance of 1 to 2 days of transport time from Kongju and Gosan. It means that more dust particles can be removed by gravity sedimentation during transport (Maring et al., 2003; Gong et al., 2003). Another reason may be that more anthropogenic pollution particles are mixed into these Asian dust plume because of the longer transport times (Kanayama et al., 2002; Noh et al., 2014; Shin et al., 2015).

Figure 8 shows the averaged values of the vertically resolved β_P, the values of δ_P^L, and the weighted values of δ_P^L ($\delta_P^L W$) measured by lidar for each group. The backscatter coefficients generally decrease with height. However, high values are found in the upper atmosphere in those cases in which δ_P^L is high. Values of δ_P^L are as high as 0.1 in group 1 and increase with increasing group number (from group 1 to group 6). The increase of the values of δ_P^L is more obvious above 2-km height than below 2-km height above ground. The higher values above 2-km above ground may be caused by the fact that Asian dust has a relatively lower chance of being mixed with other pollutants if it is transported in the upper parts of the

atmosphere (Shin et al., 2015). Especially, group 5 and group 6 show high values of δ_P^L, i.e. larger than 0.3 above 2-km height.

We see that the β_P shows different trends in these two groups. Group 5 has low values of β_P and high values of δ_P^L. In contrast, group 6 shows high values of β_P and high values of δ_P^L. This different behavior in these two groups is clearly visible in the values of $\delta_P^L W$. Values of $\delta_P^L W$ in group 5 are less than 2 throughout the whole altitude range. Values of $\delta_P^L W$ are larger than 2 in group 6.

Based on our discussion in the previous section we concluded that δ_P^S at 1020 nm may serve a qualitative indicator of the presence of mineral dust, and that values of δ_P^S at 1020 nm are large for high dust concentrations and small for low dust concentrations, see Figures 4, 7, and 8. This means that δ_P^S can be used to retrieve the dust ratio in mixed dust plumes even if vertically-resolved information on the linear particle depolarization ratio is not available.

3.3. Correlation between δ_P^S and single-scattering albedo

One main purpose of our study is to estimate the mixing ratio of dust particles with other pollutants in the atmosphere by analyzing the parameter δ_P^S. Another purpose of our study is to use δ_P^S as the basis parameters for estimating the variation of the optical and microphysical properties of dust when it mixes with anthropogenic pollution particles. Correlations between δ_P^S and other optical parameters allow us to gain insight into these variations.

Variations of aerosol absorption properties can be described by the single-scattering albedo

(SSA). The variability of light-absorption of aerosol mixtures discussed in this contribution allows us to assess the direct forcing of mixed-dust plumes. We can also investigate the semi-direct forcing that may occur from atmospheric heating by absorbing aerosol layers (Noh et al., 2012b; 2016b; Noh, 2014). We also investigate how SSA varies with the volume particle size distribution. For these investigations we use the values of δ_P^S.

Figure 9 depicts the AERONET-derived SSA and the volume particle size distributions for each of the 6 groups, respectively. The SSA-spectra vary with changing δ_P^S in clearly distinguishable patterns. The SSA spectra of group 1 (low δ_P^S) show that SSA decreases with increasing wavelength. We find that SSA decreases with increasing measurement wavelength for particle plumes that are dominated by urban-industrial and biomass-burning particles (Dubovik et al., 2002; Giles et al., 2012). Black carbon particles have the strongest light-absorption capacity in the near-infrared wavelength region.

In contrast, the SSA spectra of group 6 (high δ_P^S) show an increase of SSA with increasing wavelength. The wavelength dependence (i.e. increasing, decreasing, or constant with wavelength) of SSA is an important property that is used in aerosol type classification because the spectral absorption characteristics depend on aerosol type (Giles et al., 2012; Russell et al., 2010; Eck et al., 2010; 2005; Dubovik et al., 2002).

The increase of SSA with increasing wavelength is a characteristic optical feature of desert dust particles (Giles et al., 2012). Dust exhibits strong light-absorption in the ultraviolet (UV) and at short visible wavelengths (e.g., 440 nm) and lower light-absorption from mid-visible to near infrared wavelengths (Sokolik and Toon, 1999).

Kim et al. (2011) define particles with å < 0.2 as “pure dust” based on observations of dust particles over North Africa and the Arabian Peninsula. The average value of SSA of the “pure

dust" part of the aerosol plumes observed at the four observation sites is 0.91, 0.97, 0.97, and 0.97 at 440, 675, 870, and 1020 nm wavelength, respectively.

The SSA spectra of Group 6 at Kongju, Gosan and Osaka resemble the SSA spectra of "pure dust" described by Kim et al. (2011). The SSA of group 6 at Kongju and Gosan show similar values reported by Kim et al. (2011), i.e. 0.94, 0.98, 0.98, and 0.99 at 440, 675, 870, and 1020 nm wavelength, respectively. Lower values of SSA are observed at Osaka. We find 0.88, 0.95, 0.96, and 0.95 at 440, 675, 870, and 1020 nm wavelength, respectively. The differences of SSA at Osaka may be caused by the mixing of pollution particles with dust.

Except for the SSA at 440 nm, the SSA at 675, 870, and 1020 nm show higher values for high δ_p^S. This increase of SSA with increasing δ_p^S results from the mixing of fine-mode pollution particles with coarse-mode Asian dust.

Mixtures of desert dust and pollution aerosols contain two primary particulate light-absorbing species, black carbon in fine-mode particles (Bond and Bergstrom, 2006) and iron oxides in coarse-mode dust particles (Sokolik and Toon, 1999). Iron oxides cause strong light-absorption in the UV and in the short-wavelength range of the visible spectral range of light (Derimian et al., 2008). In pollution particles the principal absorber is soot or black carbon which exhibits light-absorption throughout the entire solar spectrum, because the imaginary part of the complex refractive index shows comparably little wavelength dependence (Bergstrom et al., 2002).

The SSA as a function of δ_p^S at the Seoul and Gosan sites shows very little variation at 440 nm compared to the other wavelengths we considered in our study (675, 870, and 1020 nm). Eck et al. (2010) suggest that this low variation of SSA at 440 nm is induced when both, coarse-mode-aerosol dominated mixtures (desert dust) and fine-mode-dominated aerosol

mixtures (pollution) have relatively similar magnitudes of light-absorption compared to their light-scattering capacity at that wavelength.

The variations of the fine-mode and the coarse-mode part of the size distributions are clearly shown in Figure 9. Group 1 contains fine-mode-dominated particle size distributions. The fine-mode part of the particle size distributions decreases and the coarse-mode part of the size distributions increases for increasing δ_P^S. The variations of Cv_c/Cv_f for each group listed in Table 2 show these tendencies more clearly.

The values of Cv_c/Cv_f increase as we move from group 1 to 6. The values of Cv_c/Cv_f in group 1 are similar at Seoul, Kongju, Gosan, and Osaka. We find 0.29, 0.32, 0.35, and 0.28, respectively. The values of Cv_c/Cv_f are similar for all three observation sites for each of the groups 1 - 5.

However, in the case of group 6, Cvc/Cvf is 7.6, 11.3, and 8.6 at Kongju, Gosan, and Osaka, respectively. The values of Cv_c/Cv_f in group 6 are smaller than the average value at Dunhuang. The average value of Cv_c/Cv_f at Dunhuang is 15.0 ± 2.6, see Table 4. Cv_c/Cv_f decreases if fine-mode pollution particles are mixed into a dust plume and/or if coarse-mode dust particles are removed from the plume during long-range transport.

3. 4. δ_P^S, SSA, and particle size distribution at the dust source region

We analyzed the AERONET Sun/sky radiometer data taken in the source region of Asian dust and evaluated the optical properties and δ_P^S of "pure Asian dust". Figure 10 shows δ_P^S, SSA and volume particle size distributions observed on 5 days in one of the source regions of Asian dust, i.e. Dunhuang in 2012. Values of δ_P^S at 440 nm are characteristic of pure dust particles, i.e. we find values larger than 0.25. SSA increases with increasing measurement

wavelength which is also characteristic of pure dust. We find this behavior on all days except for the data representing 8 April 2012. We find that the SSA at each wavelength (at the Dunhuang site) is higher than the SSA retrieved at the corresponding wavelengths for sites in North Africa and the Arabian Peninsula (Kim et al., 2011; Müller et al., 2010).

Table 3 lists aerosol optical depth (τ) at 500 nm, the optical-depth-related Ångström ex ponent (å) for the wavelength range from 440 – 870 nm, the absorption-related Ångst röm exponent ($å_A$) for that same wavelength range, the coarse-mode fraction of the v olume concentration (CMF_{vc}), and the dust ratio (R_D) derived on the basis of δ_P^S at 10 20 nm. The values of å observed at Dunhuang on all measurement dates used in this study indicate the presence of pure dust, as suggested by Kim et al. (2011). The exception is the measurement on 8 April 2012. On that day, we find a value of 0.25 for δ_P^S at 1020 nm and a vaue of 1.76 for $å_A$. These values are comparably lower than the values retrieved for the other observation days. In addition, volume particle size distributions retrieved for 8 April (see Figure 10) show a higher value of the modal volume radius for the coarse-mode size distribution compared to what is typically found for size distributions of desert dust (Dubovik et al. 2002; Müller et al., 2010; 2012). We conclude that particles observed on 8 April 2012 describe a mixed-dust plume rather than a pure dust plume.

We compare the average values of δ_P^S, SSA, and the volume particle size distributions observed at Dunhuang with the respective values of group 6 at Kongju, Gosan, and Osaka. We exclude the data taken on 8 April 2012 at Dunhuang in the calculation of the average values because that data likely do not represent pure Asian dust.

Figure 11 shows our comparison results. The highest values of δ_P^S at Dunhuang are 0.26, 0.28, 0.30, and 0.33 at 440, 675, 870, and 1020 nm wavelength, respectively. The spectral

behavior of δ_P^S (at the four wavelengths) at Kongju, Gosan, and Osaka is similar to the spectral behavior of δ_P^S retrieved for the Dunhuang site. However, the values of δ_P^S at the four measurement wavelengths at Kongju, Gosan, and Osaka are 0.04 - 0.05 lower than the respective values at the Dunhuang site. This difference between Dunhuang and the other three sites may be caused by gravitational settling of coarse mode dust particles during transport and/or by a higher share of anthropogenic pollution particles that may enter the dust plume during long-range transport from the source region to the other three sites.

The volume particle size distributions shown in Figure 11 (c) corroborate our assumption. The volume concentration of the coarse mode particles is as low as 0.36, 0.44, and 0.33 ($\mu m^3/\mu m^2$) in the far-field sites of Kongju, Gosan, and Osaka, respectively. We find that among all days during which we observed pure Asian dust at Dunhuang, the minimum value of 0.49 ($\mu m^3/\mu m^2$) was found on 9 April 2012, see Figure 11 (c) and Table 4.

Figure 11 (b) shows a comparison of the spectral SSA between Dunhuang and the other three sites. The average values of SSA at Dunhuang are 0.94, 0.98, 0.98, and 0.98 at 440, 675, 870, and 1020 nm, respectively. The value of 0.94 for SSA at 440 nm at the Dunhuang site is higher than the SSA of “pure dust” observed over North Africa and the Arabian Peninsula (Kim et al., 2011; Müller et al., 2011; Müller et al., 2010).

As noticed previously, iron oxides cause the strongest light-absorption in the ultraviolet and at visible wavelengths (Derimian et al., 2008). We assume that the differences of SSA at 440 nm between the Dunhuang site and observation sites in North Africa and the Arabian Peninsula are caused by differences of the chemical composition of dust particles, as for example by the concentration of iron oxides in dust particles at these sites.

Our results show that nearly-pure dust may be transported to Kongju and Gosan from long

distances, and that the coarse mode fraction of the particle size distribution may not necessarily increase in that case. The spectral behavior of SSA and its values at each wavelength at the Kongju and Gosan sites which are long-range transport sites match the values of SSA at Dunhuang. This match suggests that the dust at these three sites may have a similar chemical composition and perhaps also a similar concentration of iron oxide.

SSA values at Osaka are lower than those at Kongju and Gosan. We find values of 0.88, 0.95, 0.96, and 0.95 at 440, 675, 870, and 1020 nm, respectively. These low SSAs can be caused by the presence of pollution particles. We first investigate the vertical distribution of the dust plumes of group 6 at Osaka. The vertical distribution of particles in the dust plumes of group 6 at Osaka can be clearly distinguished according to their observation date.

Figure 12 shows the separated values of β_P, δ_P^L, and $\delta_P^L W$ (dust and non-dust contribution) in terms of case 1 and 2 for group 6 at Osaka on the basis of the observation date. The data taken on 14 and 15 March 2010 (case 1) show that the dust plumes are distributed up to 3.5 km height above ground. The main part of the dust plumes is located between 1 and 2 km height on both days. The values of δ_P^L are above 0.25 in that height range. The β_P-values of the dust plume are lower below 1 km height compared to what we find for β above 1 km above ground. The value of δ_P^L varies between 0.1 and 0.12 and thus is lower compared to what we find between 1 and 2 km height.

The dust plumes extend to 2 km height above ground on 2 May 2011 (measurement case 2). We find high values of β_P near the surface. Values of 0.3 – 0.4 for δ_P^L are higher than depolarization ratios found for case 1.

Case 1 is quite different from case 2 if we look at $\delta_P^L W$. The values of $\delta_P^L W$ of case 1 are

mainly affected by Asian dust that is present above 1 km height above ground. Values for case 2 are mainly influenced by Asian dust near the surface.

The differences of main aerosol height may be one reason why the light-absorption capacity of the aerosols described by these two cases differs. There is a higher possibility that with regard to case 2 pollutants can be mixed during long-range transport.

Figure 13 corroborates our assumption. Figure 13 shows values of δ_P^S, SSA, and volume particle size distributions for two cases. The values of δ_P^S and SSA in case 1 show similar values compared to the case of pure dust observed at Dunhuang. Values of these parameters are different from those at Dunhuang for case 2. Particularly, the values of SSA of case 2 are significantly lower than SSA-values at Dunhuang. Moreover, SSAs at 1020 nm are lower than those at 870 nm for case 2. This differences of the absolute values and the differences of the spectral behavior may be caused by the mixing of dust with light-absorbing pollutants, such as black carbon, when we take account of the vertical distribution of the dust plume; see Figure 12.

The differences of $å_A$ between case 1 and case 2 (Table 5) corroboratet this observation. The value of $å_A$ in case 1 is 2.12 which points to pure dust. In contrast, the value of $å_A$ of case 2 is 1.58 which is more likely representative of a mixture of dust with pollutants (Russell et al., 2010).

Figure 14 shows backward trajectories. The transport pattern is different for case 1 and case 2. The main portions of the dust plumes of case 1 passed at heights above 1.5 – 2 km over source regions of major pollution emissions in China and Korea, i.e., above the planetary boundary layer, before the plumes arrived over Osaka. Since most of the pollution resides in the PBL the possibility is low that the main dust layer mixed with pollutants.

In contrast to case 1, case 2 indicates that pollutants were mixed into the Asian dust layers while they were transported near the surface and within the PBL over industrialized areas and before they arrived over Osaka. Shin et al. (2015) reported that more pollution particles can be mixed into dust plumes if these plumes are transported at low altitude above ground.

3. 5. Retrieval of Dust ratio using Sun/sky radiometer derived Depolarization ratio

The concept of separating lidar backscatter signals resulting from the contribution of dust particles in mixed dust plumes to the total backscatter signals using δ_p has already been applied to lidar measurements (Shimizu et al., 2004; Noh, 2014; Tesche et al., 2009). In the case of AERONET Sun/sky radiometer data R_D is calculated from Eq. (2) (see section 2) and the use of δ_P^S at 1020 nm. The retrieved R_D is compared with CMF_{vc}. The comparison between R_D retrieved from AERONET data and CMF_{vc} allows us to distinguish between non-dust coarse-mode particles and dust.

Figure 15 shows the correlation between R_D and CMF_{vc} in terms of R^2. We find a comparably high correlation between R_D and CMF_{vc}. Values are 0.72, 0.95, 0.77, and 0.93 at Seoul, Kongju, Gosan, and Osaka, respectively.

R_D describes the ratio of dust particles to other types of non-spherical aerosols in the atmosphere. Unlike R_D, CMF_{vc} considers the size of particles and is not correlated to the shape of the particles. Since most of the dust particles belong to the coarse-mode fraction, the value of CMF_{vc} increases alongside with the dust ratio. However, the coarse-mode of a particle size distribution does not include dust only but also contains large particles that are

generated by physical and chemical reactions, e.g. coagulation, condensation processes, and hygroscopic growth.

Figure 15 shows that CMF_{vc} is on average 0.12-0.17 higher than R_D at the four observation sites, which implies that non-dust particles are present, i.e., even though dust particles for the most part belong to the coarse-mode fraction of particle size distributions, not all coarse-mode particles are dust particles. The average values of CMF_{vc} and the differences between R_D and CMF_{vc} for each of the 6 groups are listed in Table 1.

R_D of groups 1 – 5 is 0.11 - 0.19 lower than CMF_{vc} at the four sites. The differences between R_D and CMF_{vc} are lower for group 6. We find 0.4, 0.4, and 0.3 at Kongju, Gosan, and Osaka, respectively.

We find a similar difference for the Dunhuang site, see Table 3. The average values of R_D and CMF_{vc} are 0.97 ± 0.02 and 0.94 ± 0.01, respectively, except for the case of 8 April. This means that most of the coarse-mode particles are composed of dust particles. However, pollution and/or biomass burning particles can be injected into the dust plume during transport from the source region. These particles may contribute to the coarse mode of the volume particle size distribution. If the dust plume is transported at low altitude above ground, there is an increased possibility that dust mixes with other aerosols (Shin et al., 2015).

This increased possibility is corroborated by the results for the case of Osaka, see group 6. Table 5 shows for this case that δ_P^S, SSA, and the particle size distribution clearly depend on the altitude of the dust plume. R_D and CMF_{vc} show very similar values with respect to case 1. The average value of the difference between R_D and CMF_{vc} is 0.004 ± 0.008 for the case that the main part of the dust plume is transported above the planetary boundary layer (case 1). This difference between R_D and CMF_{vc} increases to 0.11 ± 0.04 when the dust plume is

transported near the surface, as can be seen from δ_P^L W of case 2. From these results we can infer that the coarse mode is mostly composed of pure dust particles without that mixing with other types of particle occurred during transport above the PBL. However, the ratio of dust particles to non-dust coarse-mode particles decreases as the result of mixing processes during transport. These phenomena can be explained by the variation of the volume median radius (Rv).

The volume median radius of the coarse mode (Rv_c) of 3.21-3.27 μm for urban-industrial aerosols generated by fossil fuel combustion and biomass burning aerosols produced by forest and grassland fires is higher than the Rv_c of 2.62-3.05 μm of desert dust particles (Dubovik et al., 2002; Eck et al., 2010). In this study, Rv_c shows low values when the observed particles are nearly pure dust. The average Rv_c at Dunhuang is 1.88 μm (except 8 April 2012). This value is quite similar to 2 μm of Rv_c for dust that originated from China and which was measured over Japan (Tanaka et al., 1989). The average Rv_c at Osaka decreases from 2.85 to 1.85 μm between group 1 and group 6, respectively. The other sites show the same pattern of decreasing values between groups 1 to 6. The average Rv_c of 2.15 at Kongju and 1.77 μm at Gosan (group 6) also shows values that are similar to the values found in the dust source region. The average Rv_c of the other groups is higher than Rv_c of dust in the source region. We find the highest values in group 1, i.e. 3.05, 2.72, 2.58, and 2.85 μm at Seoul, Kongju, Gosan, and Osaka, respectively.

4. Summary and Conclusion

In this study we investigated the reliability of the linear particle depolarization ratio (δ_P^S) that is derived by AERONET Sun/sky radiometers. This parameter can be used for detecting dust

particles. We compared data obtained from AERONET to the linear particle depolarization ratios measured by lidar (δ_P^L). We considered low (cases dominated by pollution particles) to high linear particle depolarization ratios (cases dominated by Asian dust) at four downwind regions (Seoul, Kongju, Gosan and Osaka) of Asian dust. We calculated the column-integrated weighted δ_P^L (δ_P^{CL}) and compared these values with δ_P^S. The strongest correlation exists between δ_P^S at 1020 nm and δ_P^{CL}. However, that latter value was measured at 532 nm. Values are 0.90, 0.92, 0.79, and 0.89 for the sites at Seoul, Kongju, Gosan, and Osaka, respectively. The correlation decreased with decreasing wavelength that was used by the AERONET instrument. The correlation coefficient was 0.89, 0.92, 0.76, and 0.88 at 870 nm at Seoul, Kongju, Gosan, and Osaka, respectively. The correlation at 675 nm is even weaker. We find values of 0.81, 0.90, 0.64, and 0.81 at Seoul, Kongju, Gosan, and Osaka, respectively. The correlation coefficient at 440 nm is significantly lower. We find values of 0.38, 0.62, 0.26, and 0.28 at Seoul, Kongju, Gosan, and Osaka, respectively. We assume that the low correlation is related to the size of fine-mode particles. However, more data are needed in order to better understand the reasons for the low correlation at 440 nm.

Despite the discrepany of the lidar ratios measured with lidar and inferred from AERONET sunphotometer we are of the opinion that δ_P^S at 1020 nm can be used as a parameter to estimate the variation of optical and microphysical properties of dust when it is mixed with anthropogenic pollution particles. There is a clear pattern of variation of the fine and coarse modes of the volume particle size distributions in the context of changes of the value of δ_P^S at 1020 nm. Fine-mode dominant volume particle size distributions are present for low values of δ_P^S at 1020 nm. The fine-mode fraction of the volume particle size distribution decreases

and the coarse-mode fraction of the particle size distribution increases when the δ_P^S at 1020 nm increases.

The SSA spectra show clearly distinguishable patterns when compared to the variation of δ_P^S at 1020 nm. The SSA decreases with increasing measurement wavelength for low values of δ_P^S at 1020 nm. In contrast, the SSA increases with increasing wavelength for high values of δ_P^S at 1020 nm.

The dust ratio (R_D) can be derived from the δ_P^S at 1020 nm. The R_D is approximately 0.12 to 0.17 lower than what we find from the coarse-mode fraction of the volume concentration (CMF_{vc}). However, if δ_P^S at 1020 nm is larger than 0.25, then R_D is similar to the value of CMF_{vc}, and the difference between these two parameters is less than 0.04. We conclude that the values of δ_P^S at 1020 nm can be used to estimate the dust ratio. The dust ratio estimated in that way can then be used as basic information that could allow us to calculate the mass concentration of Asian dust and air pollutants in terms of column-integrated values.

We conclude that on the basis of this first study values of δ_P^S at 1020 nm provide comparably reliable information with regard to identifying the presence of Asian dust particles in mixed aerosol plumes. The values of δ_P^S at 1020 nm are high for high dust concentrations and small for low dust concentrations. This means that δ_P^S at 1020 nm can be used to retrieve the dust ratio in mixed dust plumes.

Regardless of these findings we will carry out more studies in order to confirm these preliminary results. We also need to keep in mind that we cannot identify the vertical distribution of dust particles on the basis of δ_P^S because δ_P^S is a column-integrated value.

Acknowledgement

This work was funded by the Korea Meteorological Administration Research and Development Program under Grant KMIPA 2015-6150. This work was supported by a National Research Foundation of Korea (NRF) grant funded by the Korean government (MEST) (NRF-2015R1D1A1A09058269). This research was also supported by the International Environmental Research Center (IERC). Lidar data were provided by courtesy of AD-Net (http://www-lidar.nies.go.jp/AD-Net).

References

Alfaro, S. C., Lafon, S., Rajot, J. L., Formenti, P., Gaudichet, A. and Maillé, M.: Iron oxides and light absorption by pure desert dust: An experimental study, J. Geophys. Res., 109(D8), D08208, doi:10.1029/2003JD004374, 2004.

Ansmann, A., et al.: Ash and fine-mode particle mass profiles from EARLINET-AERONET observations over central Europe after the eruptions of the Eyjafjallajökull volcano in 2010, J. Geophys. Res., 116, D00U02,doi:10.1029/2010JD015567., 2011.

Behrendt, A. and Nakamura, T.: Calculation of the calibration constant of polarization lidar and its dependency on atmospheric temperature, Opt. Express, OE, 10(16), 805–817, doi:10.1364/OE.10.000805, 2002.

Bergstrom, R. W., Russell, P. B., and Hignett, P.: Wavelength dependence of the absorption of black carbon particles: Predictions and results from the TARFOX experiment and implications for the aerosol single scattering albedo, J. Atmos. Sci., 59, 567–577, 2002.

Bohren, C. F. and Huffman, D. R.: Absorption and Scattering by a Sphere, in Absorption and Scattering of Light by Small Particles, pp. 82–129, Wiley-VCH Verlag GmbH. [online] Available from: http://onlinelibrary.wiley.com/doi/10.1002/9783527618156.ch4/summary (Accessed 27 December 2016), 1983.

Bond, T. C. and Bergstrom, R. W.: Light Absorption by Carbonaceous Particles: An Investigative Review, Aerosol Science and Technology, 40(1), 27–67, doi:10.1080/02786820500421521, 2006.

Bravo-Aranda, J. A., Titos, G., Granados-Munoz, M. J., GuerreroRascado, J. L., Navas-Guzman, F., Valenzuela, A., Lyamani, H., Olmo, F. J., Andrey, J., and Alados-Arboledas, L.: Study of mineral dust entrainment in the planetary boundary layer by lidar depolarisation technique, Tellus B, 67, 26180, doi:10.3402/tellusb.v67.26180, 2015.

Burton, S. P., Ferrare, R. A., Vaughan, M. A., Omar, A. H., Rogers, R. R., Hostetler, C. A. and Hair, J. W.: Aerosol classification from airborne HSRL and comparisons with the CALIPSO vertical feature mask, Atmos. Meas. Tech., 6(5), 1397–1412, doi:10.5194/amt-6-1397-2013, 2013.

Burton, S.P., Vaughan, M.A., Ferrare, R.A., Hostetler, C.A.: Separating mixtures of aerosol types in airborne High Spectral Resolution Lidar data. Atmos. Meas. Tech. 7, 419-436. 2014.

Cairo, F., Donfrancesco, G. D., Adriani, A., Pulvirenti, L. and Fierli, F.: Comparison of various linear depolarization parameters measured by lidar, Appl. Opt., AO, 38(21), 4425–4432, doi:10.1364/AO.38.004425, 1999.

Chin, M., Diehl, T., Dubovik, O., Eck, T. F., Holben, B. N., Sinyuk, A. and Streets, D. G.: Light absorption by pollution, dust, and biomass burning aerosols: a global model study and evaluation with AERONET measurements, Ann. Geophys., 27(9), 3439–3464, doi:10.5194/angeo-27-3439-2009, 2009.

Derimian, Y., Karnieli, A., Kaufman, Y. J., Andreae, M. O., Andreae, T. W., Dubovik, O., Maenhaut, W. and Koren, I.: The role of iron and black carbon in aerosol light absorption, Atmos. Chem. Phys., 8(13), 3623–3637, doi:10.5194/acp-8-3623-2008, 2008.

Dubovik, O., Holben, B., Eck, T. F., Smirnov, A., Kaufman, Y. J., King, M. D., Tanré, D. and Slutsker, I.: Variability of Absorption and Optical Properties of Key Aerosol Types Observed in Worldwide Locations, J. Atmos. Sci., 59(3), 590–608, doi:10.1175/1520-0469(2002)059<0590:VOAAOP>2.0.CO;2, 2002.

Dubovik, O., Sinyuk, A., Lapyonok, T., Holben, B. N., Mishchenko, M., Yang, P., Eck, T. F., Volten, H., Muñoz, O., Veihelmann, B., van der Zande, W. J., Leon, J.-F., Sorokin, M. and Slutsker, I.: Application of spheroid models to account for aerosol particle nonsphericity in remote sensing of desert dust, J. Geophys. Res., 111(D11), D11208, doi:10.1029/2005JD006619, 2006.

Eck, T. F., Holben, B. N., Reid, J. S., Dubovik, O., Smirnov, A., O'Neill, N. T., Slutsker, I. and Kinne, S.: Wavelength dependence of the optical depth of biomass burning, urban, and desert dust aerosols, J. Geophys. Res., 104(D24), 31333–31349, doi:10.1029/1999JD900923, 1999.

Eck, T. F., Holben, B. N., Dubovik, O., Smirnov, A., Goloub, P., Chen, H. B., Chatenet, B., Gomes, L., Zhang, X.-Y., Tsay, S.-C., Ji, Q., Giles, D. and Slutsker, I.: Columnar aerosol optical properties at AERONET sites in central eastern Asia and aerosol transport to the tropical mid-Pacific, J. Geophys. Res., 110(D6), D06202, doi:10.1029/2004JD005274, 2005.

Eck, T. F., Holben, B. N., Sinyuk, A., Pinker, R. T., Goloub, P., Chen, H., Chatenet, B., Li, Z., Singh, R. P., Tripathi, S. N., Reid, J. S., Giles, D. M., Dubovik, O., O'Neill, N. T., Smirnov, A., Wang, P. and Xia, X.: Climatological aspects of the optical properties of fine/coarse mode aerosol mixtures, J. Geophys. Res., 115(D19), D19205, doi:10.1029/2010JD014002, 2010.

Fernald, F. G.: Analysis of atmospheric lidar observations- Some comments, Applied optics, 23, 652–653, 1984.

Freudenthaler, V., Esselborn, M., Wiegner, M., Heese, B., Tesche, M., Ansmann, A., Müller, D., Althausen, D., Wirth, M., Fix, A., Ehret, G., Knippertz, P., Toledano, C., Gasteiger, J., Garhammer, M. and Seefeldner, M.: Depolarization ratio profiling at several wavelengths in pure Saharan dust during SAMUM 2006, Tellus B, 61(1), 165–179, doi:10.1111/j.1600-0889.2008.00396.x, 2009.

Giles, D. M., Holben, B. N., Eck, T. F., Sinyuk, A., Smirnov, A., Slutsker, I., Dickerson, R. R., Thompson, A. M. and Schafer, J. S.: An analysis of AERONET aerosol absorption properties and classifications representative of aerosol source regions, J. Geophys. Res., 117(D17), D17203, doi:10.1029/2012JD018127, 2012.

Gong, S. L., Zhang, X. Y., Zhao, T. L., McKendry, I. G., Jaffe, D. A. and Lu, N. M.: Characterization of soil dust aerosol in China and its transport and distribution during 2001 ACE-Asia: 2. Model simulation and validation, J. Geophys. Res., 108(D9), 4262, doi:10.1029/2002JD002633, 2003.

Haarig. M., Ansmann, A., Althausen, D., Klepel, A., Groβ, S., Freudenthaler, V., Toledano, C., Mamouri. R-E., Farrell, D. A., Prescod, D. A., Marnou, E., Burton, S. P., Gasteiger, J., Engelmann, R., and Baars, H.: Triple-wavelength depolarization-ratio profiling of Saharan dust over Barbados during SALTRACE in 2013 and 2014, Atmos. Chem. Phys. Discuss, doi:10.5194/acp-2017-170, 2017

Haywood, J. M., Allan, R. P., Culverwell, I., Slingo, T., Milton, S., Edwards, J. and Clerbaux, N.: Can desert dust explain the outgoing longwave radiation anomaly over the Sahara during July 2003?, J. Geophys. Res., 110(D5), D05105, doi:10.1029/2004JD005232, 2005.

Holben, B. N., Eck, T. F., Slutsker, I., Tanré, D., Buis, J. P., Setzer, A., Vermote, E., Reagan, J. A., Kaufman, Y. J., Nakajima, T., Lavenu, F., Jankowiak, I. and Smirnov, A.: AERONET—A Federated Instrument Network and Data Archive for Aerosol Characterization, Remote Sensing of Environment, 66(1), 1–16, doi:10.1016/S0034-4257(98)00031-5, 1998.

Husar, R. B., Tratt, D. M., Schichtel, B. A., Falke, S. R., Li, F., Jaffe, D., Gassó, S., Gill, T., Laulainen, N. S., Lu, F., Reheis, M. C., Chun, Y., Westphal, D., Holben, B. N., Gueymard, C., McKendry, I., Kuring, N., Feldman, G. C., McClain, C., Frouin, R. J., Merrill, J., DuBois, D., Vignola, F., Murayama, T., Nickovic, S., Wilson, W. E., Sassen, K., Sugimoto, N. and Malm, W. C.: Asian dust events of April 1998, J. Geophys. Res., 106(D16), 18317–18330, doi:10.1029/2000JD900788, 2001.

IPCC: Climate Change 2013 - The Physical Science Basis: Working Group I Contribution to the Fifth Assessment Report of the Intergovernmental Panel on Climate Change [Stocker, T.F., D. Qin, G.-K. Plattner, M. Tignor, S.K. Allen, J. Boschung, A. Nauels, Y. Xia, V. Bex

and P.M. Midgley (eds.)], Cambridge University Press Cambridge, UK, and New York, NY, USA., 2013.

Iwasaka, Y., Shibata, T., Nagatani, T., Shi, G.-Y., Kim, Y. S., Matsuki, A., Trochkine, D., Zhang, D., Yamada, M., Nagatani, M., Nakata, H., Shen, Z., Li, G., Chen, B. and Kawahira, K.: Large depolarization ratio of free tropospheric aerosols over the Taklamakan Desert revealed by lidar measurements: Possible diffusion and transport of dust particles, J. Geophys. Res., 108(D23), 8652, doi:10.1029/2002JD003267, 2003.

Jickells, T. D., An, Z. S., Andersen, K. K., Baker, A. R., Bergametti, G., Brooks, N., Cao, J. J., Boyd, P. W., Duce, R. A., Hunter, K. A., Kawahata, H., Kubilay, N., laRoche, J., Liss, P. S., Mahowald, N., Prospero, J. M., Ridgwell, A. J., Tegen, I. and Torres, R.: Global Iron Connections Between Desert Dust, Ocean Biogeochemistry, and Climate, Science, 308(5718), 67–71, doi:10.1126/science.1105959, 2005.

Kanayama, S., Yabuki, S., Yanagisawa, F. and Motoyama, R.: The chemical and strontium isotope composition of atmospheric aerosols over Japan: the contribution of long-range-transported Asian dust (Kosa), Atmospheric Environment, 36(33), 5159–5175, doi:10.1016/S1352-2310(02)00587-3, 2002.

Kim, D., Chin, M., Yu, H., Eck, T. F., Sinyuk, A., Smirnov, A. and Holben, B. N.: Dust optical properties over North Africa and Arabian Peninsula derived from the AERONET dataset, Atmos. Chem. Phys., 11(20), 10733–10741, doi:10.5194/acp-11-10733-2011, 2011.

Kinne, S., Schulz, M., Textor, C., Guibert, S., Balkanski, Y., Bauer, S. E., Berntsen, T., Berglen, T. F., Boucher, O., Chin, M., Collins, W., Dentener, F., Diehl, T., Easter, R., Feichter, J., Fillmore, D., Ghan, S., Ginoux, P., Gong, S., Grini, A., Hendricks, J., Herzog, M., Horowitz, L., Isaksen, I., Iversen, T., Kirkevåg, A., Kloster, S., Koch, D., Kristjansson, J. E., Krol, M., Lauer, A., Lamarque, J. F., Lesins, G., Liu, X., Lohmann, U., Montanaro, V., Myhre, G., Penner, J., Pitari, G., Reddy, S., Seland, O., Stier, P., Takemura, T. and Tie, X.: An AeroCom initial assessment – optical properties in aerosol component modules of global models, Atmos. Chem. Phys., 6(7), 1815–1834, doi:10.5194/acp-6-1815-2006, 2006.

Lafon, S., Rajot, J.-L., Alfaro, S. C. and Gaudichet, A.: Quantification of iron oxides in desert aerosol, Atmospheric Environment, 38(8), 1211–1218, doi:10.1016/j.atmosenv.2003.11.006, 2004.

Lafon, S., Sokolik, I. N., Rajot, J. L., Caquineau, S. and Gaudichet, A.: Characterization of iron oxides in mineral dust aerosols: Implications for light absorption, J. Geophys. Res., 111(D21), D21207, doi:10.1029/2005JD007016, 2006.

Lee, J., Kim, J., Song, C. H., Ryu, J.-H., Ahn, Y.-H. and Song, C. K.: Algorithm for retrieval of aerosol optical properties over the ocean from the Geostationary Ocean Color Imager, Remote Sensing of Environment, 114(5), 1077–1088, doi:10.1016/j.rse.2009.12.021, 2010a.

Lee, K.-H., Muller, D., Noh, Y.-M., Shin, S.-K. and Shin, D.-H.: Depolarization Ratio Retrievals Using AERONET Sun Photometer Data, J. Opt. Soc. Korea, JOSK, 14(3), 178–184, 2010b.

Mamouri, R.-E. and Ansmann, A.: Potential of polarization lidar to separate fine dust, coarse dust, maritime, and anthropogenic aerosol profiles, Atmos. Meas. Tech., in preparation, 2017.

Maring, H., Savoie, D. L., Izaguirre, M. A., Custals, L. and Reid, J. S.: Mineral dust aerosol size distribution change during atmospheric transport, J. Geophys. Res., 108(D19), 8592, doi:10.1029/2002JD002536, 2003.

Mikami, M., Shi, G. Y., Uno, I., Yabuki, S., Iwasaka, Y., Yasui, M., Aoki, T., Tanaka, T. Y., Kurosaki, Y., Masuda, K., Uchiyama, A., Matsuki, A., Sakai, T., Takemi, T., Nakawo, M., Seino, N., Ishizuka, M., Satake, S., Fujita, K., Hara, Y., Kai, K., Kanayama, S., Hayashi, M., Du, M., Kanai, Y., Yamada, Y., Zhang, X. Y., Shen, Z., Zhou, H., Abe, O., Nagai, T., Tsutsumi, Y., Chiba, M. and Suzuki, J.: Aeolian dust experiment on climate impact: An overview of Japan–China joint project ADEC, Global and Planetary Change, 52(1–4), 142–172, doi:10.1016/j.gloplacha.2006.03.001, 2006.

Müller, D., Ansmann, A., Freudenthaler, V., Kandler, K., Toledano, C., Hiebsch, A., Gasteiger, J., Esselborn, M., Tesche, M., Heese, B., Althausen, D., Weinzierl, B., Petzold, A. and von Hoyningen-Huene, W.: Mineral dust observed with AERONET Sun photometer, Raman lidar, and in situ instruments during SAMUM 2006: Shape-dependent particle properties, J. Geophys. Res., 115(D11), D11207, doi:10.1029/2009JD012523, 2010.

Müller, D., Lee, K.-H., Gasteiger, J., Tesche, M., Weinzierl, B., Kandler, K., Müller, T., Toledano, C., Otto, S., Althausen, D. and Ansmann, A.: Comparison of optical and microphysical properties of pure Saharan mineral dust observed with AERONET Sun photometer, Raman lidar, and in situ instruments during SAMUM 2006, J. Geophys. Res., 117(D7), D07211, doi:10.1029/2011JD016825, 2012.

Müller, T., Schladitz, A., Kandler, K. and Wiedensohler, A.: Spectral particle absorption coefficients, single scattering albedos and imaginary parts of refractive indices from ground based in situ measurements at Cape Verde Island during SAMUM-2, Tellus B, 63(4), doi:10.3402/tellusb.v63i4.16348, 2011.

Navas-Guzma´avas-Guzmadoi:1ller, J. A. Bravo-Aranda, J. L. Guerrero-Rascado, M. J. Granados-Mun˜uoz, D. PeDrez-Ramı´rez, F. J. Olmo, and L. Alados-Arboledas,: Eruption of the Eyjafjallajo¨ykull Volcano in spring 2010: Multiwavelength Raman lidar measurements of sulphate particles in the lower troposphere, J. Geophys. Res. Atmos., 118, 1804–1813, doi:10.1002/jgrd.50116, 2013.

Nishizawa, T., Sugimoto, N., Matsui, I., Shimizu, A., Hara, Y., Itsushi, U., Yasunaga, K., Kudo, R., Kim, S. W.,: Ground-based network observation using Mie-Raman lidars and multi-wavelength Raman lidars and algorithm to retrieve distributions of aerosol components, J. Quant. Spectrosc. Radiat. Transf., 188, 79-93, 2017.

Noh, Y. M.: Single-scattering albedo profiling of mixed Asian dust plumes with multiwavelength Raman lidar, Atmospheric Environment, 95, 305–317, doi:10.1016/j.atmosenv.2014.06.028, 2014.

Noh, Y. M., Kim, Y. J., Choi, B. C. and Murayama, T.: Aerosol lidar ratio characteristics measured by a multi-wavelength Raman lidar system at Anmyeon Island, Korea, Atmospheric Research, 86(1), 76–87, doi:10.1016/j.atmosres.2007.03.006, 2007.

Noh, Y. M., Kim, Y. J. and Müller, D.: Seasonal characteristics of lidar ratios measured with a Raman lidar at Gwangju, Korea in spring and autumn, Atmospheric Environment, 42(9), 2208–2224, doi:10.1016/j.atmosenv.2007.11.045, 2008.

Noh, Y. M., Müller, D., Lee, H., Lee, K. and Kim, Y. J.: Columnar aerosol optical and radiative properties according to season and air mass transport pattern over East Asia, Environ Monit Assess, 184(8), 4763–4775, doi:10.1007/s10661-011-2300-7, 2012a.

Noh, Y. M., Müller, D., Lee, H., Lee, K., Kim, K., Shin, S. and Kim, Y. J.: Estimation of radiative forcing by the dust and non-dust content in mixed East Asian pollution plumes on the basis of depolarization ratios measured with lidar, Atmospheric Environment, 61, 221–231, doi:10.1016/j.atmosenv.2012.07.034, 2012b.

Noh, Y. M., Müller, D., Lee, H. and Choi, T. J.: Influence of biogenic pollen on optical properties of atmospheric aerosols observed by lidar over Gwangju, South Korea, Atmospheric Environment, 69, 139–147, doi:10.1016/j.atmosenv.2012.12.018, 2013a.

Noh, Y. M., Lee, H., Mueller, D., Lee, K., Shin, D., Shin, S., Choi, T. J., Choi, Y. J. and Kim, K. R.: Investigation of the diurnal pattern of the vertical distribution of pollen in the lower troposphere using LIDAR, Atmos. Chem. Phys., 13(15), 7619–7629, doi:10.5194/acp-13-7619-2013, 2013b.

Noh, Y. M., Shin, S.-K., Lee, K., Müller, D. and Kim, K.: Utilization of the depolarization ratio derived by AERONET Sun/sky radiometer data for type confirmation of a mixed aerosol plume over East Asia, International Journal of Remote Sensing, 37(10), 2180–2197, doi:10.1080/01431161.2016.1176274, 2016a.

Noh, Y. M., Lee, K., Kim, K., Shin, S.-K., Müller, D. and Shin, D. H.: Influence of the vertical absorption profile of mixed Asian dust plumes on aerosol direct radiative forcing over East Asia, Atmospheric Environment, 138, 191–204, doi:10.1016/j.atmosenv.2016.04.044, 2016b.

Russell, P. B., Bergstrom, R. W., Shinozuka, Y., Clarke, A. D., DeCarlo, P. F., Jimenez, J. L., Livingston, J. M., Redemann, J., Dubovik, O. and Strawa, A.: Absorption Angstrom Exponent in AERONET and related data as an indicator of aerosol composition, Atmos. Chem. Phys., 10(3), 1155–1169, doi:10.5194/acp-10-1155-2010, 2010.

Sakai, T., Nagai, T., Nakazato, M., Mano, Y. and Matsumura, T.: Ice clouds and Asian dust studied with lidar measurements of particle extinction-to-backscatter ratio, particle depolarization, and water-vapor mixing ratio over Tsukuba, Appl Opt, 42(36), 7103–7116, 2003.

Sassen, K., Wang, Z. and Liu, D.: Global distribution of cirrus clouds from CloudSat/Cloud-Aerosol Lidar and Infrared Pathfinder Satellite Observations (CALIPSO) measurements, J. Geophys. Res., 113(D8), D00A12, doi:10.1029/2008JD009972, 2008.

Shimizu, A., Sugimoto, N., Matsui, I., Arao, K., Uno, I., Murayama, T., Kagawa, N., Aoki, K., Uchiyama, A. and Yamazaki, A.: Continuous observations of Asian dust and other aerosols by polarization lidars in China and Japan during ACE-Asia, J. Geophys. Res., 109(D19), D19S17, doi:10.1029/2002JD003253, 2004.

Shimizu, A., Nishizawa, T., Jin, Y., Kim, S. W., Wang, Z., Batdorj, D., and Sugimoto, N., Evolution of a lidar network for tropospheric aeroso ldetection in East Asia, Opt. Eng., 56 (3), 2016

Shin, S.-K., Müller, D., Lee, C., Lee, K. H., Shin, D., Kim, Y. J. and Noh, Y. M.: Vertical variation of optical properties of mixed Asian dust/pollution plumes according to pathway of air mass transport over East Asia, Atmos. Chem. Phys., 15(12), 6707–6720, doi:10.5194/acp-15-6707-2015, 2015.

Sokolik, I. N. and Toon, O. B.: Incorporation of mineralogical composition into models of the radiative properties of mineral aerosol from UV to IR wavelengths, J. Geophys. Res., 104(D8), 9423–9444, doi:10.1029/1998JD200048, 1999.

Sugimoto, N., Matsui, I., Shimizu, A., Nishizawa, T., Hara, Y., Xie, C., Uno, I., Yumimoto, K., Wang, Z. and Yoon, S.-C.: Lidar network observations of tropospheric aerosols, vol. 7153, p. 71530A–71530A–13., 2008.

Sugimoto, N., Nishizawa, T., Shimizu, A., Matsui, I., and Jin, Y.: Characterization of aerosols in East Asia with the Asian Dust and Aerosol Lidar Observation Network (AD-Net), in: Proc. SPIE, vol. 9262, pp. 92 620K–92 620K–9, doi:10.1117/12.2069892, 2014

Sun, Y., Zhuang, G., Wang, Y., Zhao, X., Li, J., Wang, Z. and An, Z.: Chemical composition of dust storms in Beijing and implications for the mixing of mineral aerosol with pollution aerosol on the pathway, J. Geophys. Res., 110(D24), D24209, doi:10.1029/2005JD006054, 2005.

Sun, Y., Zhuang, G., Huang, K., Li, J., Wang, Q., Wang, Y., Lin, Y., Fu, J. S., Zhang, W., Tang, A. and Zhao, X.: Asian dust over northern China and its impact on the downstream aerosol chemistry in 2004, J. Geophys. Res., 115(D7), D00K09, doi:10.1029/2009JD012757, 2010.

Tanaka, M., Nakajima, T., Shiobara, M., Yamano, M., and Arao, K.: Aerosol optical characteristics in the yellow sand events observed in May, 1982 at Nagasaki—Part 1. Observations. J. Meteor. Soc. Japan, 67, 267–278, 1989.

Tesche, M., Ansmann, A., Müller, D., Althausen, D., Engelmann, R., Freudenthaler, V. and Groß, S.: Vertically resolved separation of dust and smoke over Cape Verde using multiwavelength Raman and polarization lidars during Saharan Mineral Dust Experiment 2008, J. Geophys. Res., 114(D13), D13202, doi:10.1029/2009JD011862, 2009.

Tesche, M., Müller, D., Gross, S., Ansmann, A., Althausen, D., Freudenthaler, V., Weinzierl, B., Veira, A. and Petzold, A.: Optical and microphysical properties of smoke over Cape Verde inferred from multiwavelength lidar measurements, Tellus B, 63(4), 677–694, doi:10.1111/j.1600-0889.2011.00549.x, 2011.

Volten, H., Muñoz, O., Rol, E., de Haan, J. F., Vassen, W., Hovenier, J. W., Muinonen, K. and Nousiainen, T.: Scattering matrices of mineral aerosol particles at 441.6 nm and 632.8 nm, J. Geophys. Res., 106(D15), 17375–17401, doi:10.1029/2001JD900068, 2001.

Whiteman, D. N., Melfi, S. H. and Ferrare, R. A.: Raman lidar system for the measurement of water vapor and aerosols in the Earth's atmosphere, Appl Opt, 31(16), 3068–3082, 1992.

Yu, X., Cheng, T., Chen, J. and Liu, Y.: A comparison of dust properties between China continent and Korea, Japan in East Asia, Atmospheric Environment, 40(30), 5787–5797, doi:10.1016/j.atmosenv.2006.05.013, 2006.

Figure captions

Figure 1. Map of the observation sites. Measurements with AERONET Sun/sky radiometer and lidar were performed at Seoul, Kongju, Gosan, and Osaka. AERONET Sun/sky radiometer measurements were made at Dunhuang.

Figure 2. Lidar derived aerosol backscatter coefficient (β_P; black line), the linear particle depolarization ratio (δ_P^L; green), and the weighted linear particle depolarization ratio (δ_P^LW; gray) at 532 nm observed (a) from 23:00 – 23:15 UTC on 13 March 2010, (b) from 06:00 – 06:15 UTC on 22 March 2010, and (c) from 23:15 - 23:30 on 3 May 2010. The wavelength of δ_P^S is 1020 nm. The height is expressed as altitude above ground level (a.g.l.)

Figure 3. Aerosol optical depth (τ) at 500 nm retrieved from AERONET Sun/sky radiometer measurements (black squares) and linear particle depolarization ratio derived at 1020 nm

from Sun/sky radiometer data (δ_P^S; blue open circles). (a) data of the four sites taken from 2010 to 2014, (b) data taken at Seoul for two years (2012 and 2013), (c) data taken at Kongju in spring 2012, and (d) data taken at Gosan during four years (2011 – 2014), mostly during spring, and (e) data taken from 2010 – 2014 at Osaka.

Figure 4. The correlation coefficients R^2 (the coefficient of determination) between δ_P^{CL} at 532 and δ_P^S at 440 (black squares), 675 (red circles), 870 (blue open triangles), and 1020 nm (orange diamonds) at (a) Seoul, (b) Kongju, (c) Gosan, and (d) Osaka.

Figure 5. The average values of δ_P^S at five wavelengths (440, 532, 670, 875, and 1020 nm) and δ_P^{CL} at 532 nm divided by the range of the differences between δ_P^S and δ_P^{CL} at 532 nm ($\delta_{P\ 532}^{CL} - \delta_{P\ 532}^{S}$). The symbol of δ_P^{CL} at 532 nm is shown as open figure and in larger size.

Figure 6. The average value of the volume size distributions derived by AERONET Sun/sky radiometer measurements divided by the range of the differences between δ_P^S and δ_P^{CL} at 532 nm ($\delta_{P\ 532}^{CL} - \delta_{P\ 532}^{S}$).

Figure 7. The average value of the δ_P^S at 440, 675, 870, and 1020 nm for each group. Each group is distinguished by color: black (group 1), red (group 2), blue (group 3), pink (group 4), gray (group 5), and orange (group 6). The average values of the δ_P^{CL} at 532 nm are shown as open circles and the same color as the values of δ_P^S.

Figure 8. Average values of the vertical profiles of (a) the particle backscatter coefficient, (b) the linear particle depolarization ratios (δ_P^L), and (c) the weighted linear particle depolarization ratios (δ_P^L w) for group 1 (1), group 2 (2), group 3 (3), group 4 (4), group 5 (5), and group 6 (6). The sites are Seoul (red), Kongju (orange), Gosan (blue), and Osaka (black).

Figure 9. Average value of the SSA and the volume particle size distributions derived from the AERONET Sun/sky radiometer measurements for each of the 6 groups considered in this study: group 1 (black), group 2 (red), group 3 (blue), group 4 (pink), group 5 (gray), and group 6 (orange).

Figure 10. (a) Linear particle depolarization ratios, (b) single-scattering albedos, and (c) volume particle size distributions derived from Sun/sky radiometer observations at Dunhuang.

Figure 11. Comparison between (a) δ_P^S, (b) SSA, and volume particle size distributions representing the dust source region (Dunhuang, black) and group-6-data (Kongju, blue), (Gosan, gray), and (Osaka, red).

Figure 12. Separation of data of group 6 at Osaka on the basis of case 1 (black) and case 2 (red). Shown are (a) backscatter coefficients, (b) linear particle depolarization ratios (δ_P^L), and (c) weighted linear particle depolarization ratios (δ_P^L W).

Figure 13. (a) δ_p^S at 440, 675, 870, and 1020 nm, (b) SSA at 440, 675, 870, and 1020 nm, and (c) volume particle size distributions. Shown are the results for case 1 (black) and case 2 (red). Cv_c/Cv_f is inserted in (c). The observation site is Osaka.

Figure 14. HYSPLIT 5-days backward trajectories of dust plumes for case 1 (a) and case 2 (…). The start height for case 1 is 1200 m (blue), 1500 m (red), and 1800 m (yellow). For case 2 it is 500 m (blue), 1000 m (red), and 1500 m (yellow). The start time is 0:00 UTC in each case.

Figure 15. Correlation plots of the dust ratio at 1020 nm versus the volume concentration in the coarse-mode fraction of the particle size distribution.

Table 1. Average value of aerosol optical depth (τ) at 500 nm, optical-depth-related Ångström exponent (å, 440 – 870 nm), absorption-related Ångström exponent ($å_A$), dust ratio (R_D) derived by δ_P^S at 1020 nm, coarse-mode fraction of the τ at 1020 nm (CMF_τ), coarse-mode fraction of the volume concentration (CMF_{vc}), and difference between CMF_{vc} and R_D (CMF_{vc} - R_D).

	DPR (1020 nm)	Group 1	Group 2	Group 3	Group 4	Group 5	Group 6	Total
		0 - 0.05	0.05 - 0.1	0.1 - 0.15	0.15 - 0.2	0.2 - 0.25	0.25 >	
Seoul	#	25	74	38	21	5		163
	τ (500 nm)	0.62 ± 0.26	0.74 ± 0.31	0.77 ± 0.29	0.62 ± 0.25	0.89 ± 0.29		0.72 ± 0.29
	å	1.42 ± 0.21	1.38 ± 0.16	1.22 ± 0.16	1.05 ± 0.12	0.8 ± 0.15		1.29 ± 0.22
	$å_A$	1.32 ± 0.37	1.56 ± 0.43	1.78 ± 0.40	1.8 ± 0.29	1.88 ± 0.36		1.62 ± 0.43
	R_D	0.08 ± 0.04	0.22 ± 0.05	0.37 ± 0.05	0.51 ± 0.05	0.63 ± 0.05		0.29 ± 0.15
	CMF_τ[1]	0.13 ± 0.06	0.29 ± 0.14	0.46 ± 0.12	0.69 ± 0.06	0.78 ± 0.02		0.37 ± 0.21
	CMF_{vc}	0.22 ± 0.06	0.38 ± 0.11	0.56 ± 0.09	0.70 ± 0.05	0.79 ± 0.06		0.45 ± 0.18
	$CMF_{vc} - R_D$	0.14	0.16	0.19	0.19	0.16		0.16
Kongju	#	1	22	8	3		10	44
	τ (500 nm)	0.67	0.68 ± 0.29	0.69 ± 0.24	0.41 ± 0.01		0.61 ± 0.21	0.65 ± 0.25
	å	1.74	1.55 ± 0.12	1.27 ± 0.16	1.09 ± 0.07		0.4 ± 0.10	1.21 ± 0.47
	$å_A$	1.25	1.32 ± 0.21	1.54 ± 0.47	1.43 ± 0.72		2.28 ± 0.29	1.58 ± 0.50
	R_D	0.08	0.21 ± 0.04	0.40 ± 0.06	0.54 ± 0.03		0.85 ± 0.06	0.41 ± 0.26
	CMF_τ[1]	0.23	0.29 ± 0.09	0.47 ± 0.16	0.66 ± 0.03		0.90 ± 0.02	0.49 ± 0.26
	CMF_{vc}	0.24	0.36 ± 0.07	0.54 ± 0.11	0.65 ± 0.01		0.88 ± 0.02	0.53 ± 0.22
	$CMF_{vc} - R_D$	0.16	0.15	0.14	0.11		0.04	0.12
Gosan	#	18	47	47	19	5	3	139
	τ (500 nm)	0.6 ± 0.24	0.54 ± 0.23	0.54 ± 0.17	0.53 ± 0.14	0.41 ± 0.02	0.85 ± 0.17	0.55 ± 0.20
	å	1.55 ± 0.14	1.34 ± 0.20	1.27 ± 0.18	0.92 ± 0.18	0.77 ± 0.11	0.24 ± 0.24	0.124 ± 0.30
	$å_A$	0.75 ± 0.36	0.91 ± 0.48	0.94 ± 0.43	0.95 ± 0.59	1.01 ± 0.11	2.39 ± 0.70	0.94 ± 0.51
	R_D	0.08 ± 0.02	0.20 ± 0.05	0.37 ± 0.04	0.53 ± 0.04	0.71 ± 0.02	0.85 ± 0.05	0.32 ± 0.18
	CMF_τ[1]	0.24 ±0.07	0.33 ± 0.15	0.53 ± 0.11	0.69 ± 0.10	0.81 ± 0.02	0.90 ± 0.02	0.47 ± 0.21
	CMF_{vc}	0.26 ± 0.06	0.37 ± 0.10	0.56 ± 0.09	0.68 ± 0.08	0.75 ± 0.05	0.89 ± 0.08	0.49 ± 0.18
	$CMF_{vc} - R_D$	0.18	0.17	0.19	0.15	0.04	0.04	0.17
Osaka	#	54	80	32	38	20	10	234
	τ (500 nm)	0.54 ± 0.21	0.47 ± 0.18	0.47 ± 0.12	0.54 ± 0.15	0.61 ± 0.17	0.58 ± 0.15	0.51 ± 0.18
	å	1.64 ± 0.13	1.52 ± 0.16	0.13 ± 0.17	1.01 ± 0.14	0.70 ± 0.18	0.26 ± 0.08	1.31 ± 0.39
	$å_A$	1.18 ± 0.25	1.23 ± 0.23	1.37 ± 0.43	1.69 ± 0.39	1.57 ± 0.43	1.98 ± 0.41	1.37 ± 0.39
	R_D	0.07 ± 0.04	0.20 ± 0.06	0.37 ± 0.06	0.55 ± 0.05	0.68 ± 0.04	0.86 ± 0.04	0.32 ± 0.23
	CMF_τ[1]	0.17 ± 0.09	0.30 ± 0.12	0.47 ± 0.14	0.69 ± 0.07	0.81 ± 0.04	0.91 ± 0.01	0.43 ± 0.26
	CMF_{vc}	0.21 ± 0.06	0.35 ± 0.07	0.52 ± 0.08	0.66 ± 0.05	0.79 ± 0.06	0.89 ± 0.03	0.45 ± 0.22
	$CMF_{vc} - R_D$	0.14	0.15	0.15	0.11	0.11	0.03	0.13

[1] 1020 nm

Table 2. Averaged volume concentration of the fine (Cv_f) and the coarse mode (Cv_c), and the ratio (Cv_c/Cv_f) for the 6 groups.

		Group 1	Group 2	Group 3	Group 4	Group 5	Group 6	Total
		0 - 0.05	0.05 - 0.1	0.1 - 0.15	0.15 - 0.2	0.2 - 0.25	0.25 >	
Seoul	Cv_f	0.112 ± 0.051	0.117 ± 0.052	0.103 ± 0.042	0.067 ± 0.032	0.082 ± 0.021		0.11 ± 0.05
	Cv_c	0.031 ± 0.013	0.069 ± 0.032	0.132 ± 0.052	0.162 ± 0.071	0.352 ± 0.172		0.098 ± 0.081
	Cv_c/Cv_f	0.29 ± 0.10	0.66 ± 0.29	1.39 ± 0.54	2.45 ± 0.65	4.26 ± 1.60		1.11 ± 0.99
Kongju	Cv_f	0.136	0.109 ± 0.044	0.092 ± 0.038	0.046 ± 0.004		0.048 ± 0.018	0.088 ± 0.044
	Cv_c	0.044	0.062 ± 0.027	0.105 ± 0.029	0.085 ± 0.012		0.361 ± 0.148	0.138 ± 0..140
	Cv_c/Cv_f	0.32	0.59 ± 0.19	1.29 ± 0.63	1.84 ± 0.12		7.61 ± 1.44	2.37 ± 2.95
Gosan	Cv_f	0.127 ± 0.043	0.104 ± 0.044	0.081 ± 0.036	0.074 ± 0.038	0.042 ± 0.002	0.054 ± 0.039	0.091 ± 0.043
	Cv_c	0.043 ± 0.016	0.059 ± 0.027	0.105 ± 0.042	0.159 ± 0.068	0.136 ± 0.059	0.444 ± 0.125	0.098 ± 0.077
	Cv_c/Cv_f	0.35 ± 0.12	0.63 ± 0.31	1.40 ± 0.57	2.36 ± 0.89	3.18 ± 1.21	11.26 ± 7.07	1.41 ± 1.92
Osaka	Cv_f	0.103 ± 0.037	0.077 ± 0.030	0.065 ± 0.019	0.066 ± 0.018	0.059 ± 0.016	0.039 ± 0.008	0.076 ± 0.031
	Cv_c	0.027 ± 0.011	0.040 ± 0.015	0.072 ± 0.028	0.135 ± 0.047	0.253 ± 0.147	0.326 ± 0.094	0.087 ± 0.097
	Cv_c/Cv_f	0.28 ± 0.11	0.56 ± 0.18	1.13 ± 0.35	2.04 ± 0.43	4.49 ± 2.58	8.49 ± 2.55	1.49 ± 2.10

Table 3. Aerosol optical depth (τ) at 500 nm, linear particle depolarization ratio (δ_P^S) derived from the sun/sky radiometer data, optical-depth-related Ångström exponent ($\mathring{a}$, 440-870 nm), absorption-related Ångström exponent ($\mathring{a}_A$), coarse-mode fraction in terms of the volume concentration (CMF_{vc}), and dust ratio (R_D) at 1020 nm. The observation site is Dunhuang.

Date	τ (500 nm)	δ_P^S (1020 nm)	$\mathring{a}$ (440-870 nm)	$\mathring{a}_A$	CMF_{vc}	R_D
8 Apr.	0.71	0.25	0.13	1.76	0.94	0.77
9 Apr.	0.92	0.31	0.12	2.17	0.93	0.94
26 Apr.	1.17	0.32	0.14	2.14	0.94	0.96
27 Apr.	1.00	0.34	0.15	2.46	0.95	0.99
28 Apr.	1.16	0.32	0.17	2.19	0.93	0.96
Ave.[1]	0.97 ± 0.17	0.31 ± 0.03	0.14 ± 0.02	2.14 ± 0.25	0.94 ± 0.01	0.93 ± 0.09
Ave.[2]	1.04 ± 0.11	0.33 ± 0.01	0.14 ± 0.02	2.24 ± 0.15	0.94 ± 0.01	0.97 ± 0.02

[1]Averaged for all data [2]Averaged except 8 Apr. data

Table 4. Volume concentration of the fine (Cv_f) and the coarse mode (Cv_c), and the ratio (Cv_c/Cv_f) at Dunhuang

Date	8 Apr.	9 Apr.	26 Apr.	27 Apr.	28 Apr.	Ave.[1]	Ave.[2]
Cv_f	0.03	0.037	0.048	0.038	0.051	0.041 ± 0.01	0.044 ± 0.01
Cv_c	0.44	0.49	0.77	0.7	0.64	0.61 ± 0.14	0.65 ± 0.12
Cv_c/Cv_f	14.8	13.2	16	18.3	12.6	14.9 ± 2.3	15.0 ± 2.6

[1]Averaged for all data [2]Averaged except 8 Apr. data

Table 5. Parameters for cases 1 and 2 for group 6 at Osaka, linear particle depolarization ratio (δ_p^S) at 440, 675, 870, and 1020 nm derived from the Sun/sky radiometer data, absorption-related Ångström exponent ($å_A$), coarse-mode fraction on the basis of the volume concentration (CMF_{vc}), and dust ratio (R_D) at 1020 nm.

	δ_P^S				$å_A$	CMF_{vc}	R_D
	440 nm	675 nm	870 nm	1020 nm			
Case 1	0.19 ± 0.02	0.24 ± 0.01	0.27 ± 0.01	0.29 ± 0.01	2.12 ± 0.38	0.87 ± 0.01	0.88 ± 0.02
Case 2	0.15 ± 0.02	0.24 ± 0.01	0.26 ± 0.01	0.27 ± 0.01	1.58 ± 0.09	0.92 ± 0.01	0.81 ± 0.03

Figure 1

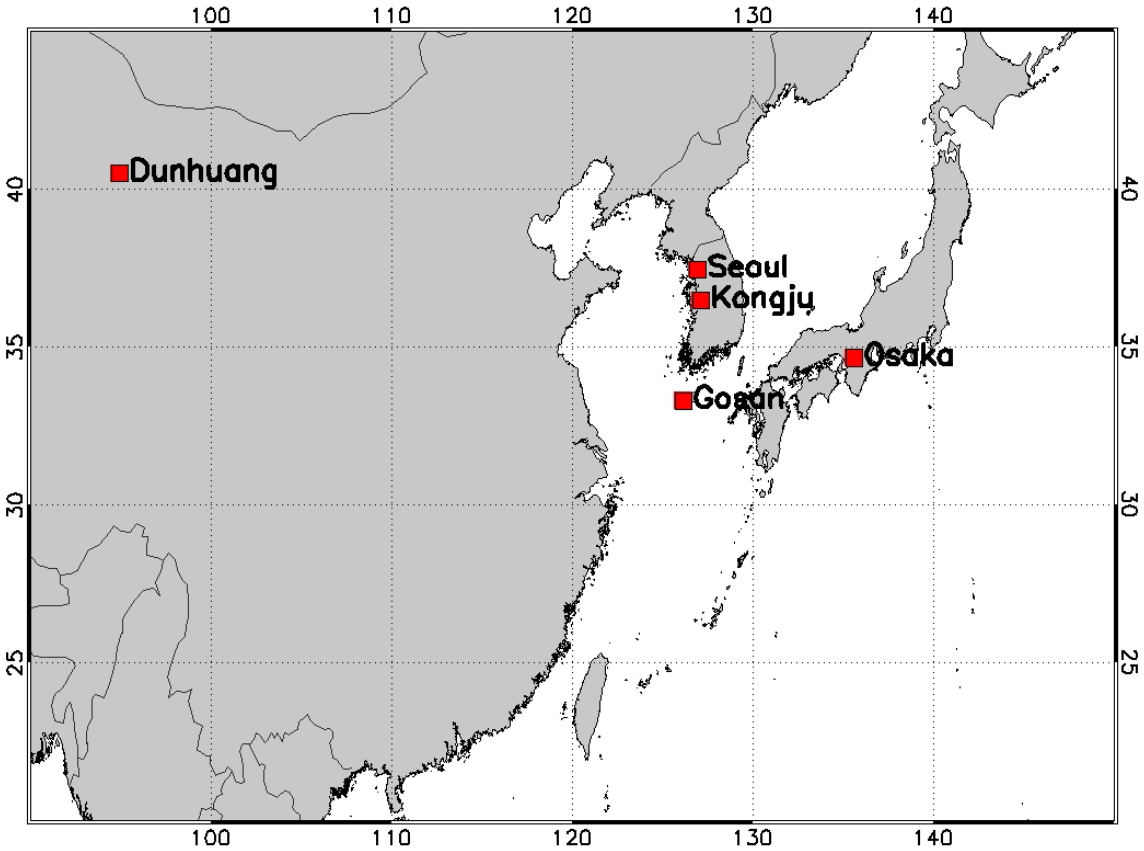
100
110
120
130
140
40
35
30
25
Dunhuang
Seoul
Kongjy
Osaka
Gosan

Figure 2

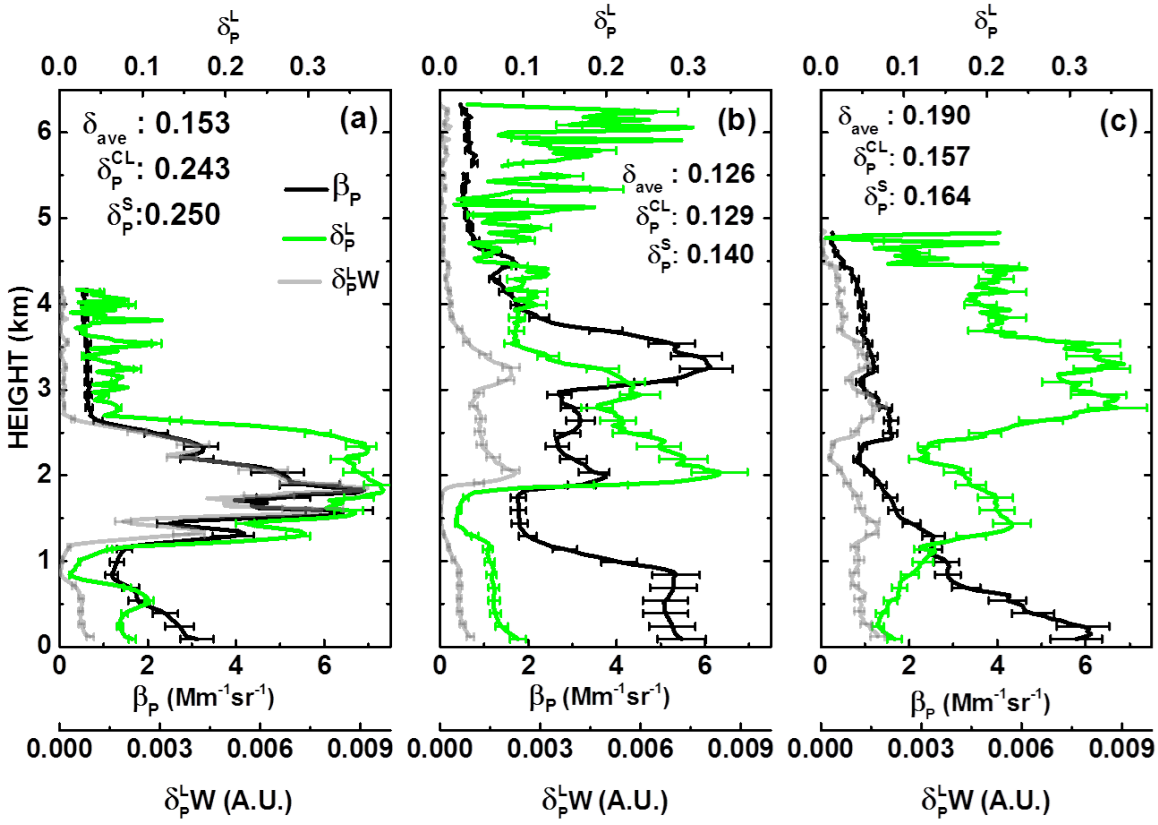
(a)
(b)
(c)
δave : 0.153
δPCL: 0.243
δPS:0.250
δave : 0.126
δPCL: 0.129
δPS: 0.140
δave : 0.190
δPCL: 0.157
δPS: 0.164
βP
δPL
δPLW
HEIGHT (km)
βP (Mm-1sr-1)
δPLW (A.U.)
δPL

Figure 3

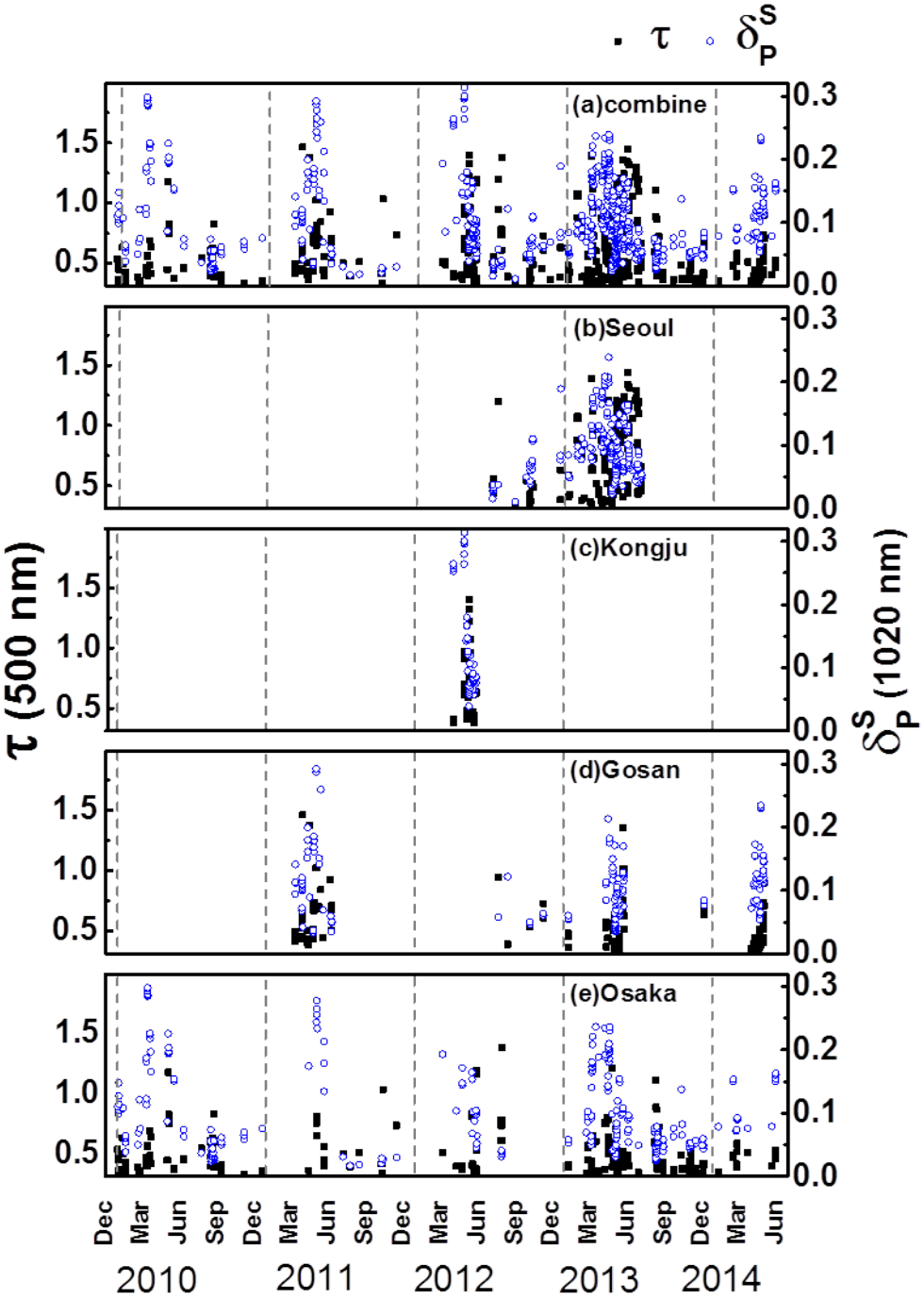
τ
δ_P^S
(a)combine
(b)Seoul
(c)Kongju
(d)Gosan
(e)Osaka
τ (500 nm)
δ_P^S (1020 nm)
0.5
1.0
1.5
0.0
0.1
0.2
0.3
Dec
Mar
Jun
Sep
2010
2011
2012
2013
2014

Figure 4

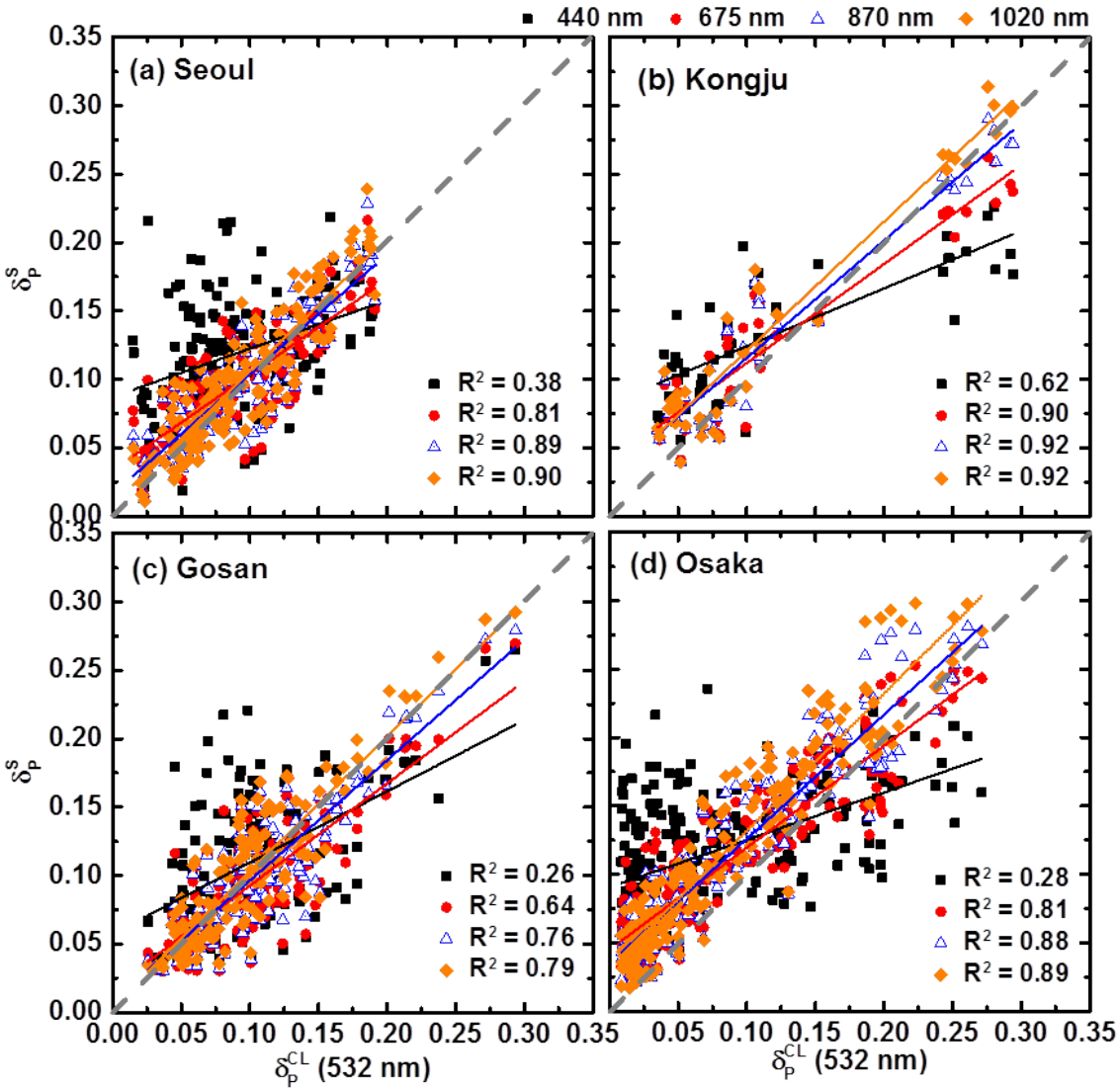
440 nm
675 nm
870 nm
1020 nm
(a) Seoul
R² = 0.38
R² = 0.81
R² = 0.89
R² = 0.90
(b) Kongju
R² = 0.62
R² = 0.90
R² = 0.92
R² = 0.92
(c) Gosan
R² = 0.26
R² = 0.64
R² = 0.76
R² = 0.79
(d) Osaka
R² = 0.28
R² = 0.81
R² = 0.88
R² = 0.89
δ_P^S
δ_P^CL (532 nm)

Figure 5

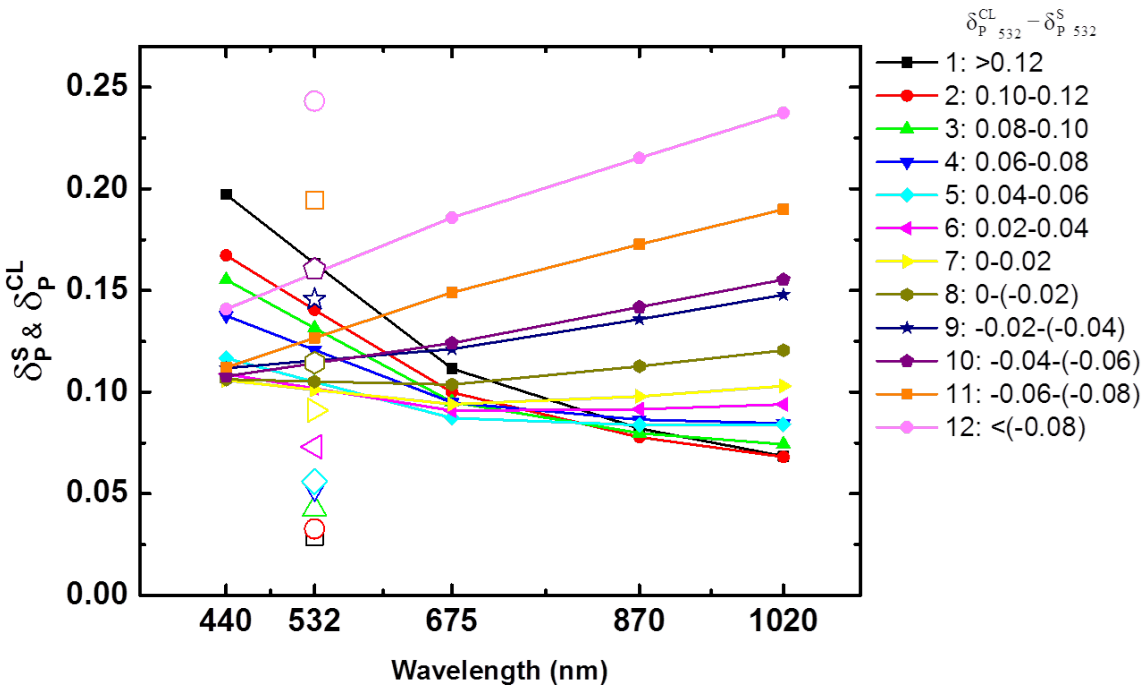
$\delta_{P\ 532}^{CL} - \delta_{P\ 532}^{S}$
1: >0.12
2: 0.10-0.12
3: 0.08-0.10
4: 0.06-0.08
5: 0.04-0.06
6: 0.02-0.04
7: 0-0.02
8: 0-(-0.02)
9: -0.02-(-0.04)
10: -0.04-(-0.06)
11: -0.06-(-0.08)
12: <(-0.08)
δ_P^S & δ_P^{CL}
0.25
0.20
0.15
0.10
0.05
0.00
440
532
675
870
1020
Wavelength (nm)

Figure 6

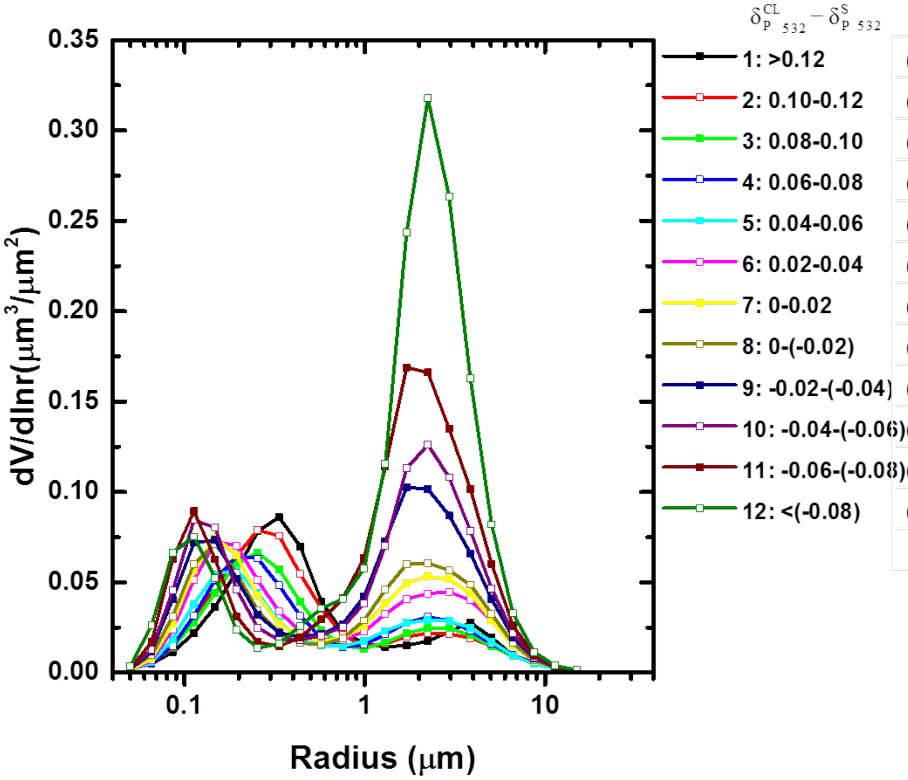

$\delta^{CL}_{p\ 532} - \delta^{S}_{p\ 532}$	Rv_f	Rv_c
1: >0.12	0.28±0.03	2.83±0.49
2: 0.10-0.12	0.26±0.03	2.82±0.50
3: 0.08-0.10	0.24±0.03	2.71±0.38
4: 0.06-0.08	0.22±0.03	2.59±0.44
5: 0.04-0.06	0.19±0.03	2.44±0.45
6: 0.02-0.04	0.19±0.03	2.49±0.45
7: 0-0.02	0.17±0.03	2.38±0.38
8: 0-(-0.02)	0.16±0.02	2.38±0.44
9: -0.02-(-0.04)	0.16±0.02	2.27±0.49
10: -0.04-(-0.06)	0.15±0.02	2.35±0.47
11: -0.06-(-0.08)	0.14±0.01	2.12±0.34
12: <(-0.08)	0.13±0.01	2.33±0.26

Figure 7

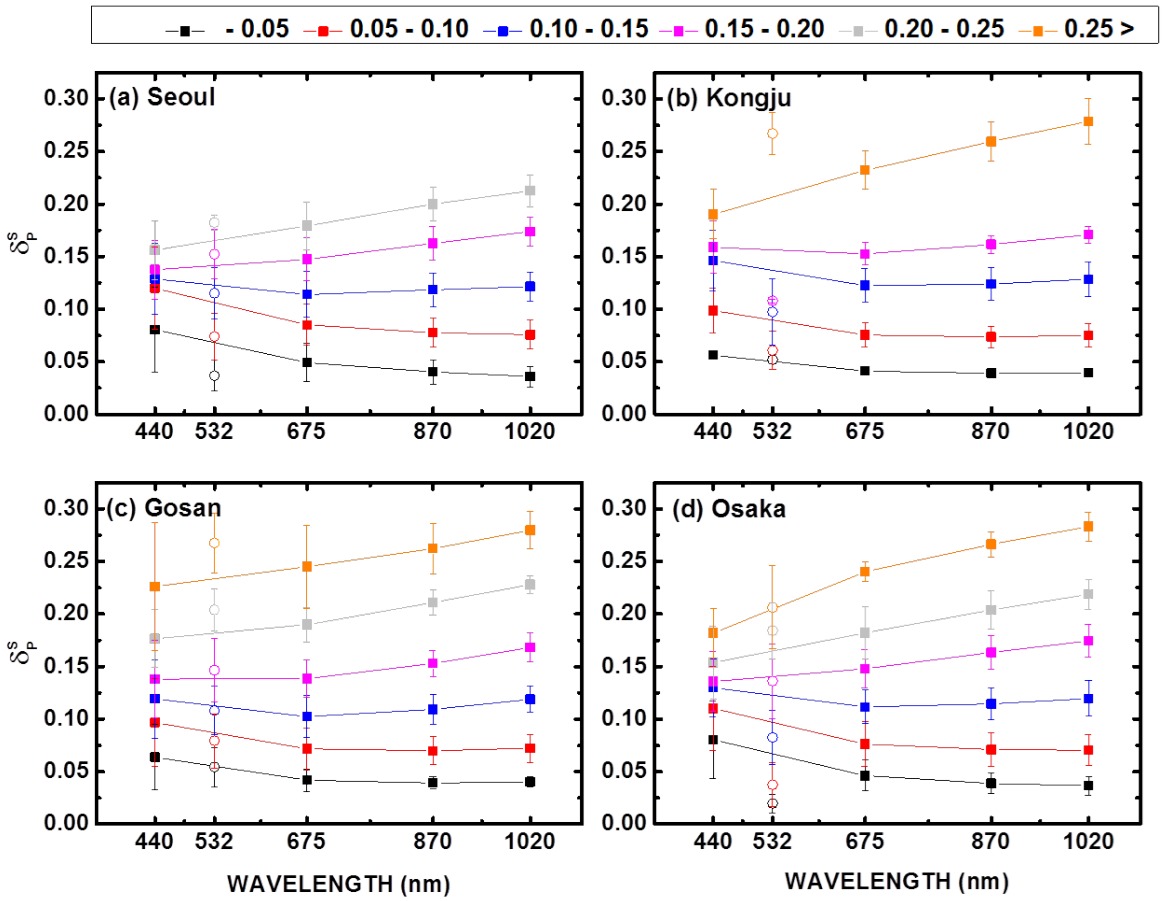
- 0.05
0.05 - 0.10
0.10 - 0.15
0.15 - 0.20
0.20 - 0.25
0.25 >
(a) Seoul
(b) Kongju
(c) Gosan
(d) Osaka
δ_P^S
0.00
0.05
0.10
0.15
0.20
0.25
0.30
440
532
675
870
1020
WAVELENGTH (nm)

Figure 8

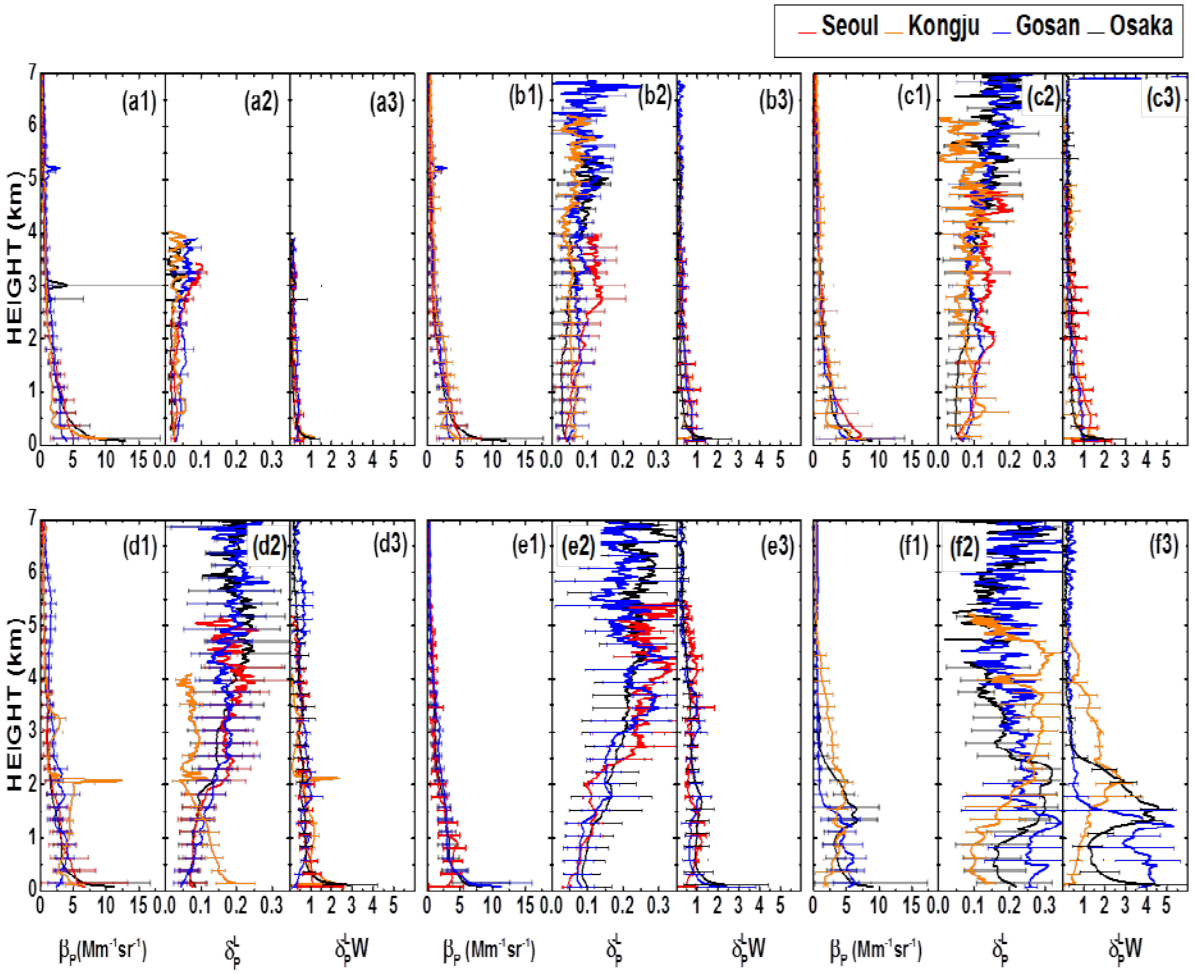
Seoul
Kongju
Gosan
Osaka
HEIGHT (km)
(a1)
(a2)
(a3)
(b1)
(b2)
(b3)
(c1)
(c2)
(c3)
(d1)
(d2)
(d3)
(e1)
(e2)
(e3)
(f1)
(f2)
(f3)
β_P(Mm^{-1}sr^{-1})
δ_P^L
δ_P^LW

Figure 9

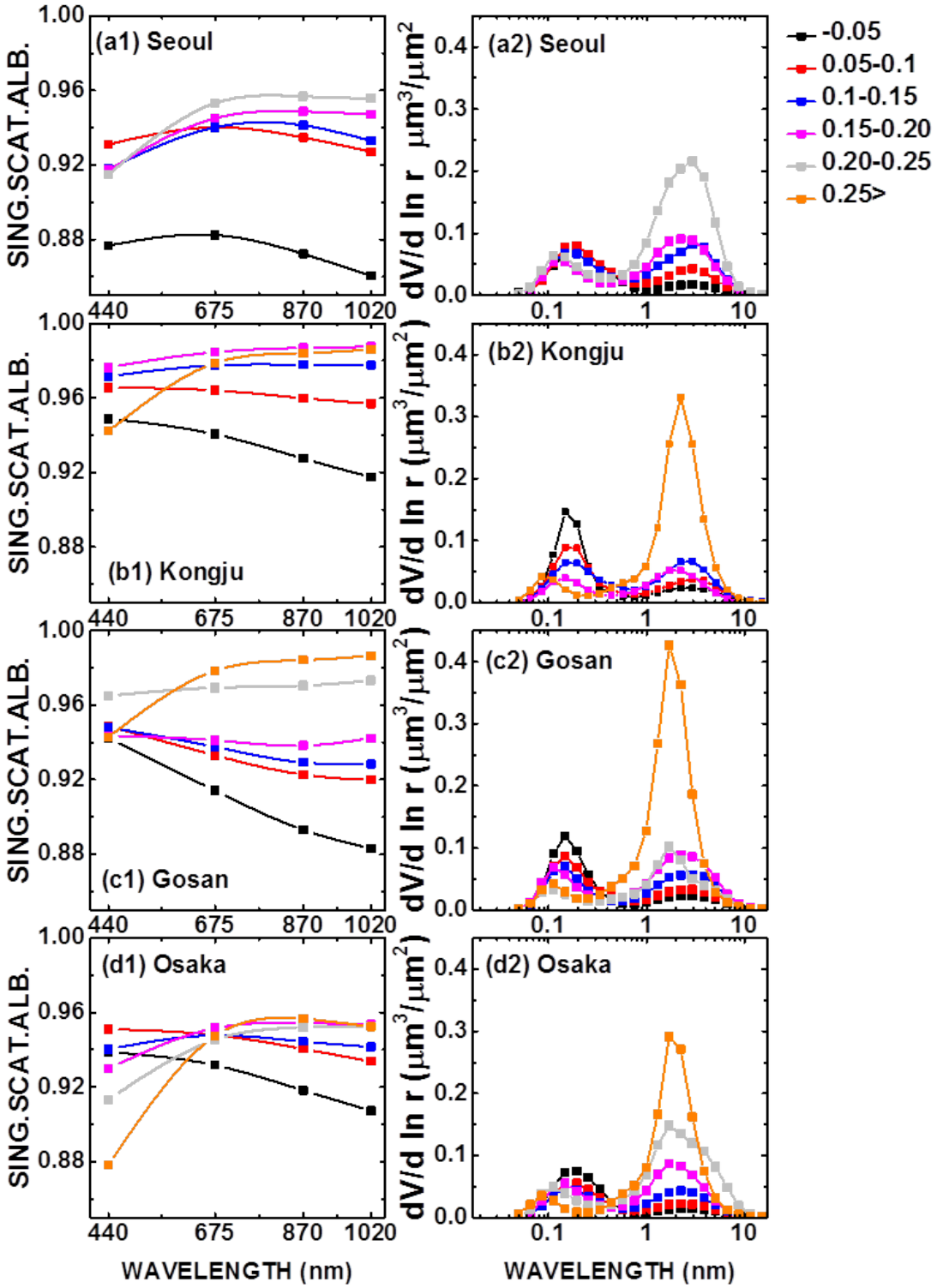
(a1) Seoul
(a2) Seoul
(b1) Kongju
(b2) Kongju
(c1) Gosan
(c2) Gosan
(d1) Osaka
(d2) Osaka
SING.SCAT.ALB.
dV/d ln r μm³/μm²
WAVELENGTH (nm)
-0.05
0.05-0.1
0.1-0.15
0.15-0.20
0.20-0.25
0.25>

Figure 10

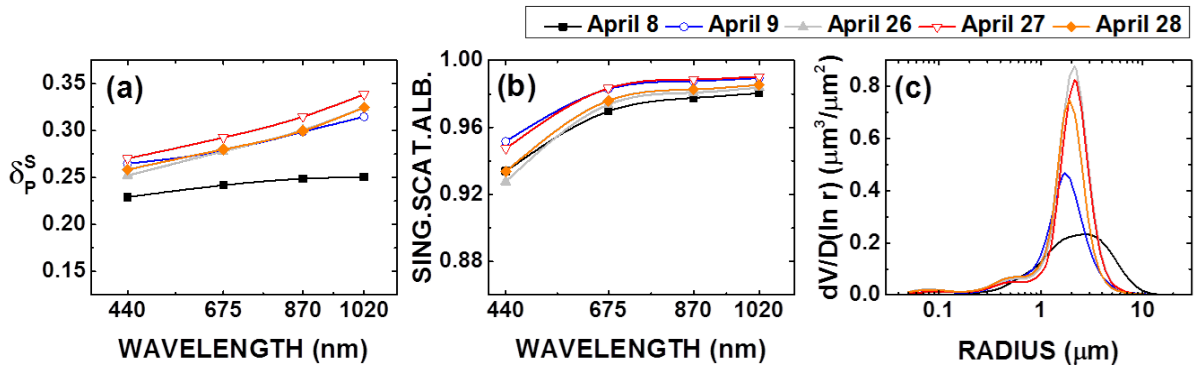

Figure 11

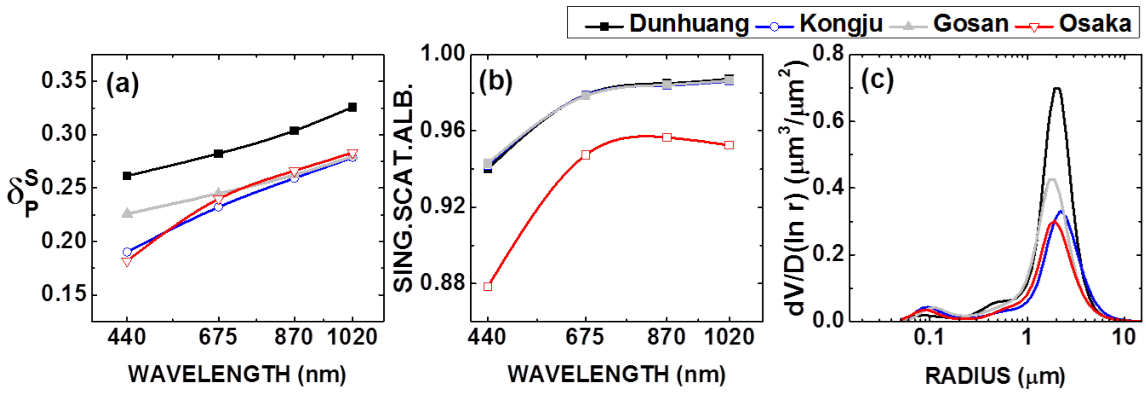

Figure 12

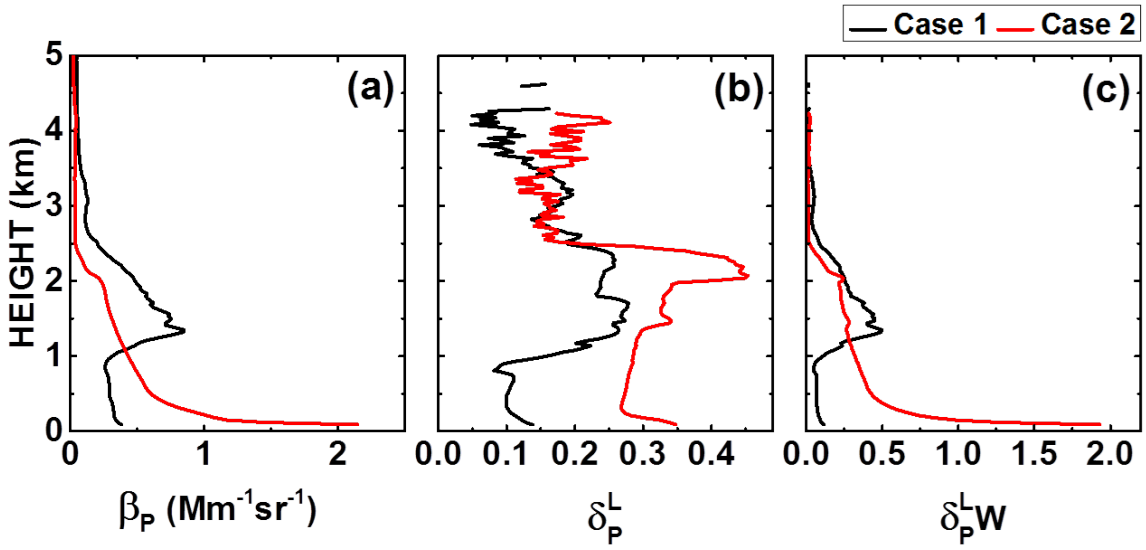

Figure 13

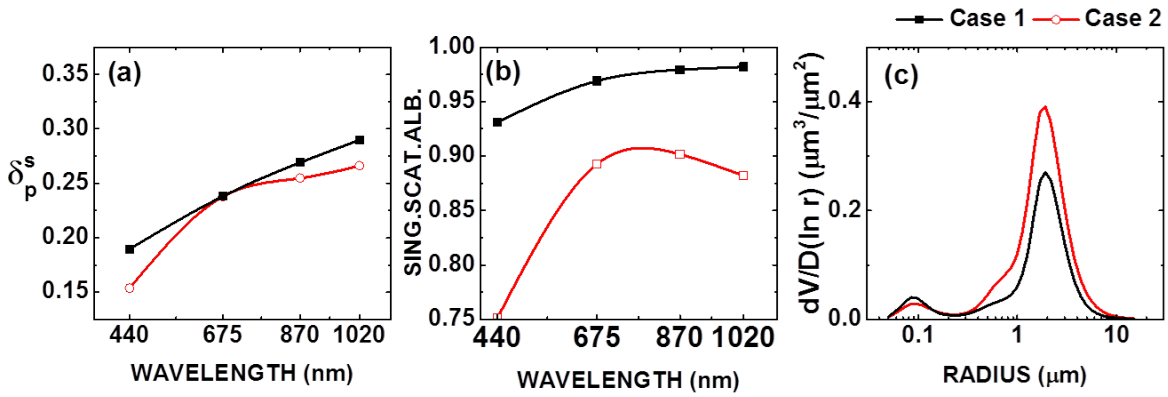

Figure 14

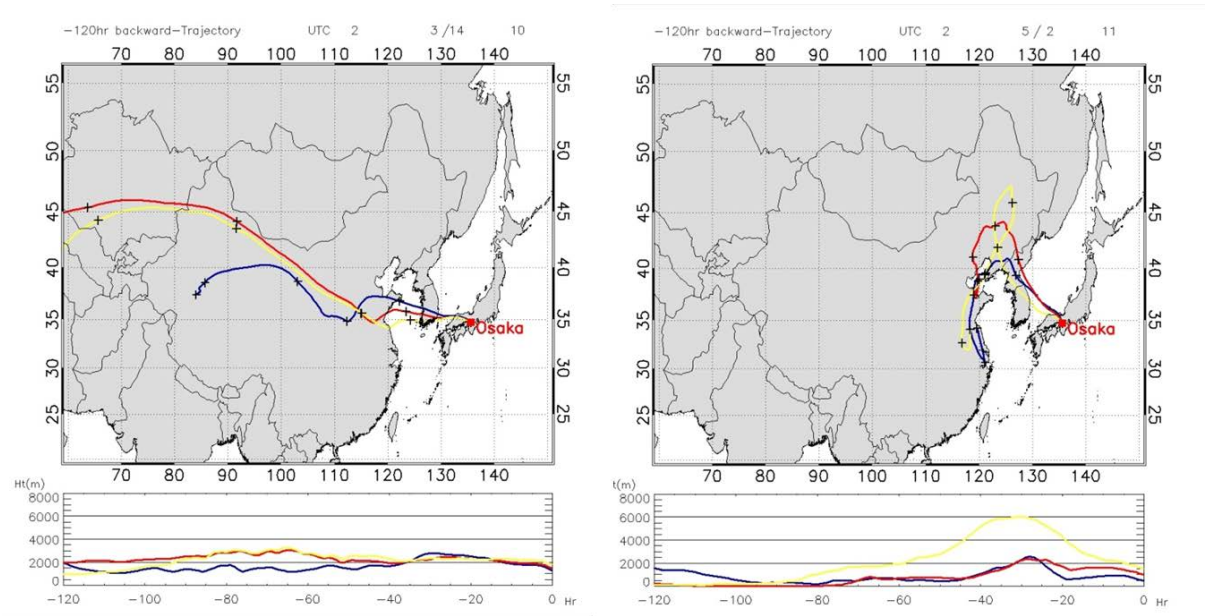
−120hr backward−Trajectory UTC 2 3 /14 10
Osaka
Ht(m)
Hr
−120hr backward−Trajectory UTC 2 5 / 2 11
Osaka
t(m)
Hr

Figure 15

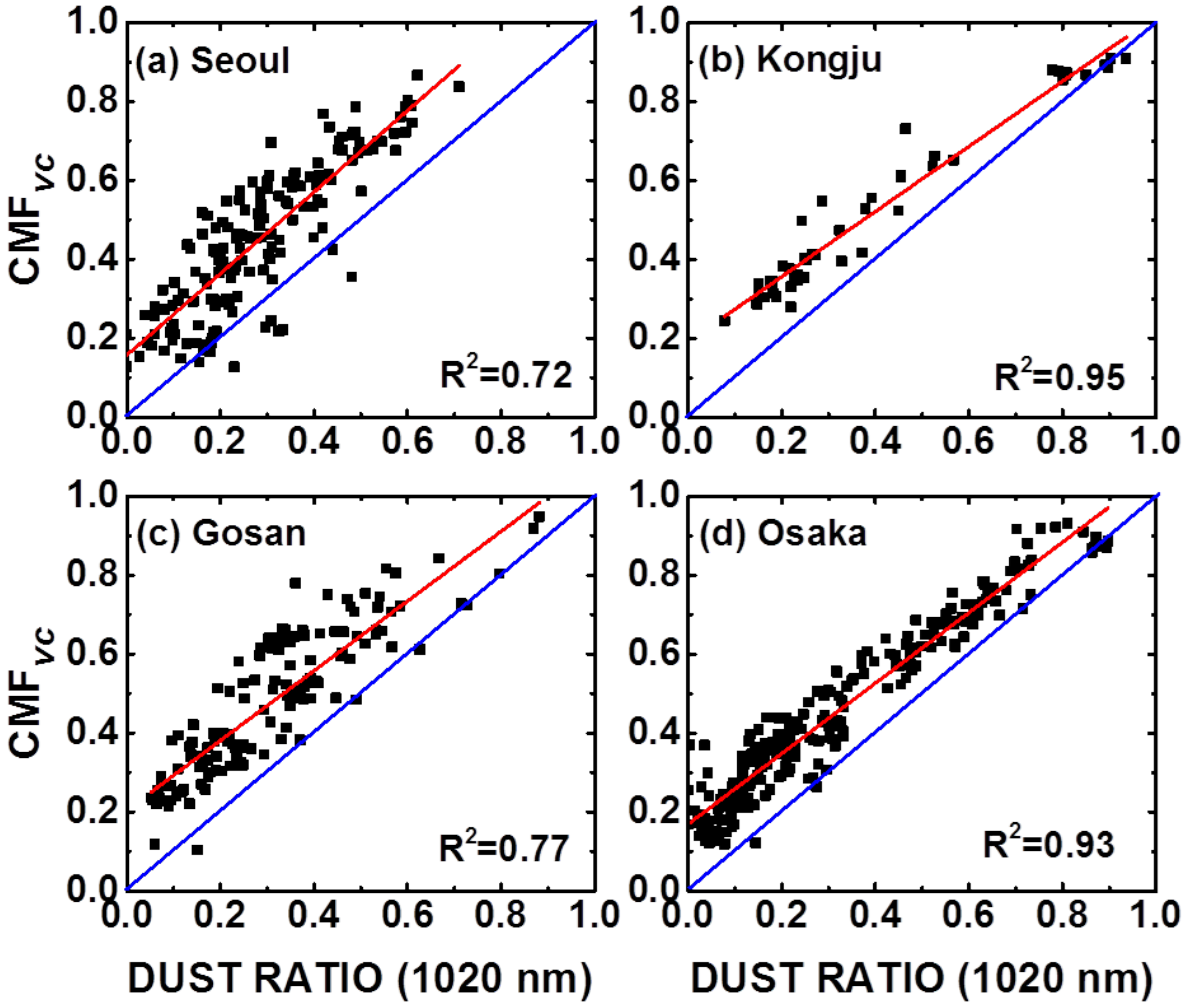
(a) Seoul
(b) Kongju
(c) Gosan
(d) Osaka
R2=0.72
R2=0.95
R2=0.77
R2=0.93
CMFvc
DUST RATIO (1020 nm)
0.0
0.2
0.4
0.6
0.8
1.0